Naval Research Laboratory
Washington, DC 20375-5320

NRL/7630/MR—2023/1

An Approach to Determine O and N_2 Densities in the Thermosphere Using EUV Airglow

RICHARD M. TUMINELLO
ANDREW W. STEPHAN

Geospace Science and Technology Branch
Space Science Division

February 22, 2023

REPORT DOCUMENTATION PAGE

Form Approved OMB No. 0704-0188

1. REPORT DATE *(DD-MM-YYYY)* 22-02-2023	**2. REPORT TYPE** NRL Memorandum Report	**3. DATES COVERED** *(From - To)* January 18, 2022 – July 31, 2022

4. TITLE AND SUBTITLE

An Approach to Determine O and N_2 Densities in the Thermosphere Using EUV Airglow

5a. CONTRACT NUMBER

5b. GRANT NUMBER

5c. PROGRAM ELEMENT NUMBER

6. AUTHOR(S)

Richard M. Tuminello and Andrew W. Stephan

5d. PROJECT NUMBER

5e. TASK NUMBER

5f. WORK UNIT NUMBER

1R33

7. PERFORMING ORGANIZATION NAME(S) AND ADDRESS(ES)

Naval Research Laboratory
4555 Overlook Avenue, SW
Washington, DC 20375-5320

8. PERFORMING ORGANIZATION REPORT NUMBER

NRL/7630/MR--2023/1

9. SPONSORING / MONITORING AGENCY NAME(S) AND ADDRESS(ES)

Naval Research Laboratory
4555 Overlook Avenue, SW
Washington, DC 20375-5320

10. SPONSOR / MONITOR'S ACRONYM(S)

NRL

11. SPONSOR / MONITOR'S REPORT NUMBER(S)

12. DISTRIBUTION / AVAILABILITY STATEMENT

DISTRIBUTION STATEMENT A: Approved for public release; distribution is unlimited.

13. SUPPLEMENTARY NOTES

14. ABSTRACT

This memorandum documents the development and validation of an algorithm designed to retrieve thermospheric atomic oxygen (O) and molecular nitrogen (N_2) densities over the altitude range 150-400 km using measurements of extreme ultraviolet (EUV) dayglow from the Ionospheric Connection Explorer (ICON). This measurement approach does not have an inherent ionospheric emission that can, under certain conditions, complicate the analysis and interpretation of these measurables using state-of-the-art far-ultraviolet (FUV) airglow measurement approach. Also, since EUV airglow emissions are produced directly by solar extreme ultraviolet rather than by the secondary process of impact by the correspondingly generated photoelectrons, this method has the potential to enable expansion of neutral density observations into the auroral zone and polar cap where the FUV measurement cannot be applied. These first results are validated by comparison to the MSIS 2.0 model, as well as contemporaneous composition and neutral density measurements from the NASA GOLD and Swarm missions. Areas for future development and improvement in the measurement and analysis of these emissions are also discussed.

15. SUBJECT TERMS

Thermosphere Composition
UV remote sensing

16. SECURITY CLASSIFICATION OF:			**17. LIMITATION OF ABSTRACT**	**18. NUMBER OF PAGES**	**19a. NAME OF RESPONSIBLE PERSON** Andrew Stephan
a. REPORT U	**b. ABSTRACT** U	**c. THIS PAGE** U	U	44	**19b. TELEPHONE NUMBER** *(include area code)* (202) 767-0211

Standard Form 298 (Rev. 8-98)
Prescribed by ANSI Std. Z39.18

This page intentionally left blank.

CONTENTS

EXECUTIVE SUMMARY E-1

1. INTRODUCTION 1

2. ICON EUV DATA 2

3. LIMB RETRIEVAL METHOD 3

4. THE EUV DAYGLOW MODEL 4
   4.1 Model Architecture 4
   4.2 Modeling the 87.8 nm Band 7
   4.3 Modeling the 61.6 nm Band 10

5. RETRIEVAL RESULTS 15
   5.1 Comparison to MSIS 00 Densities 16

6. RETRIEVAL VALIDATION 20
   6.1 MSIS 2.0 20
   6.2 Comparison to SWARM Mass Density 24
   6.3 Comparison to ICON FUV and GOLD $\Sigma O/N_2$ 25

7. EFFECTS OF USING THE CORRECTED 61.6 NM DATA 29

8. DISCUSSION 31

REFERENCES 36

FIGURES

1	Atmospheric Fit to Airglow	4
2	Diagram of the forward model geometry.	5
3	EUV 87.8 nm as Pure N	8
4	EUV 87.8 nm as a Blend of O and N	9
5	87.8 nm g-factor Histograms	10
6	86.5 Scaling vs. LT	11
7	87.8 Scaling vs. LT	11
8	Example Lookup Table	12
9	61.6 g-factor Histogram	13
10	61.6 nm Model and Data Comparison	14
11	Example Corrected 61.6 nm Profile	14
12	Distribution of F107, O, and N_2 Scalars	15
13	Comparison to MSIS 00 and MSIS 2.0 with Altitude	16
14	O Density with Latitude and LT	17
15	N2 Density with Latitude and LT	17
16	O Correlation with MSIS 00 at 200km Altitude	18
17	N_2 Correlation with MSIS 00 at 200km Altitude	19
18	O Correlation with MSIS 00 at 300km Altitude	19
19	N_2 Correlation with MSIS 00 at 300km Altitude	20
20	Comparison of MSIS 00 and MSIS 2.0	21
21	O Correlation with MSIS 2.0 at 200km Altitude	21
22	N_2 Correlation with MSIS 2.0 at 200km Altitude	22

23 O Correlation with MSIS 2.0 at 300km Altitude 22

24 N_2 Correlation with MSIS 2.0 at 300km Altitude 23

25 Retrieval Comparison to MSIS 2.0 - Local Time 24

26 Retrieval Comparison to MSIS 2.0 - Latitude 25

27 Retrieval Comparison to MSIS 2.0 - F10.7 Index 26

28 SWARM and EUV Correlation 27

29 SWARM and EUV Residuals from MSIS 28

30 FUV and EUV $\Sigma O/N_2$ Scatter 28

31 GOLD and EUV $\Sigma O/N_2$ Scatter 29

32 GOLD, ICON EUV, and ICON FUV $\Sigma O/N_2$ Time Series 30

33 GOLD, ICON EUV, and ICON FUV Daily Median $\Sigma O/N_2$ 31

34 Distribution of F107, O, and N_2 Scalars - Corrected Data 32

35 Comparison to MSIS 00 and MSIS 2.0 With Altitude - Corrected Data........ 33

36 Effects on Comparison to FUV O/N_2 34

37 Comparison to SWARM Density - Corrected Data 35

TABLES

EXECUTIVE SUMMARY

This memorandum documents the development and validation of an algorithm designed to retrieve thermospheric atomic oxygen (O) and molecular nitrogen (N_2) density profiles using measurements of extreme ultraviolet (EUV) dayglow from the Ionospheric Connection Explorer (ICON). As activity in low Earth orbit (LEO) continues to grow, it is important to characterize the environment of near-Earth space. The density of neutral species is a particularly relevant aspect of this environment, as it governs satellite drag and other surface interactions (such as erosion by atomic O). Poor modeling of neutral density has led to loss of spacecraft, for example the loss of 38 Starlink satellites in February 2022 [1]. It also is an important component of ionospheric forecast models since the prevailing composition and neutral particle densities in the thermosphere, under solar illumination, are the dominant source for generation of new plasma.

Sophisticated and robust models of thermospheric neutral density exist, such as the NRL MSIS® family of climatological models and the Thermosphere Ionosphere Electrodynamics General Circulation Model (TIE-GCM). However, much work remains to establish how the thermosphere responds to forcing from below (e.g. atmospheric tides and gravity waves) and above (e.g. solar and geomagnetic storms). One reason that this piece of the puzzle is missing is that it is difficult to make measurements of neutral density in the lower thermosphere where mass density is too high for stable in situ satellite-based measurements. A typical means of measuring lower thermospheric O and N_2 density is through the observation of far-ultraviolet (FUV) airglow of atomic oxygen at 135.6 nm and the $\mathrm{N_2}$ Lyman-Birge-Hopfield (LBH) bands (~130-180 nm), as is done on the NASA Ionospheric Connection Explorer (ICON) and Global-scale Observations of the Limb and Disk (GOLD) missions. This technique is not without limitations, however, as the FUV measurements suffer from contamination by ionospheric photochemistry at low latitudes and auroral emissions excited by precipitating energetic electrons and protons at high latitudes.

Previous work has shown the potential for making measurements of O and N_2 density in the lower-middle thermosphere using observations of extreme-ultraviolet (EUV) airglow [2]. In addition to providing another means to inform atmospheric models, this measurement approach has a potential advantage in that it does not have an inherent ionospheric emission and thus avoids the complicating factor in the state-of-the-art FUV measurement approach of accounting for this contamination source. Also, since these emissions are primarily excited directly by solar UV rather than electron impact, this method has the potential to enable expansion of neutral density observations into the auroral zone and polar cap where the FUV measurement cannot be applied.

This memorandum documents the development of a new approach and algorithm designed to retrieve thermospheric O and N_2 density from 150-400 km using measurements from the ICON EUV sensor. It summarizes the results from the validation of these first such retrieval results, and discusses the next steps in improving the algorithm.

This page intentionally left blank

AN APPROACH TO DETERMINE O AND N_2 DENSITIES IN THE THERMOSPHERE USING EUV AIRGLOW

1. INTRODUCTION

The middle thermosphere (150-400 km altitude) is an important region of near-earth space, containing the lowest orbiting artificial satellites and overlapping with the F-region ionosphere. As such, it is important to characterize this region with density and temperature measurements; however, it is difficult to make persistent in-situ mass spectrometer measurements of neutrals in this region since the high density causes orbital decay. New observations of this region have been used to continually improve the NRL MSIS® series of empirically determined thermosphere models, the most recent of which is NRLMSIS 2.0 [3]. This update addressed, in part, the demonstrated need for lowering the atomic oxygen (O) and molecular nitrogen (N_2) densities in the predecessor model NRLMSISE-00 as found by long-term analysis of measured altitude profiles of FUV airglow.[4]

One prominent means of measuring thermospheric neutrals is through observation of far-ultraviolet (FUV) dayglow. The 135.6 nm O doublet and N_2 Lyman-Birge-Hopfield bands are excited by photoelectron impact on the dayside, and limb measurements of these dayglow profiles from TIMED-GUVI have been used to retrieve profiles of O and N_2 density [4]. However, it is more common to use disk-viewing measurements of these emissions for the retrieval of $\Sigma O/N_2$, defined as the ratio of O and N_2 column density from the top of the atmosphere to a depth corresponding to an N_2 column density of 10^{17} cm^{-2} [5, 6]. This quantity is important in the study of ionosphere-thermosphere coupling since O^+ is the dominant ion in the F-region and it is often lost through charge exchange with N_2 [7]. $\Sigma O/N_2$ has been a data product on several spacecraft missions, starting with the Polar BEAR spacecraft [8] through the current Ionospheric Connection Explorer (ICON) [9] and Global-scale Observations of the Limb and Disk [10] missions.

In support of its mission to measure the connection between Earth's ionosphere and neutral atmosphere, the ICON spacecraft carries an extreme-ultraviolet (EUV) spectrometer to observe O^+ in the F-region ionosphere.[11] The ICON EUV spectral coverage spans approximately 54-88 nm at 2.4 nm resolution, while the spatial dimension is 17° wide and measures limb profiles nominally from 100-500 km, at 20 km resolution.[12] Profiles of the O^+ 61.6 nm (sometimes referred to as 61.7 nm) and 83.4 nm features are inverted to retrieve the altitude and density of the F2 peak (hmF2 and NmF2, respectively).[13] Many additional features other than these two targeted O^+ features are captured by the EUV instrument. Tuminello et al.[2] have demonstrated that the 87.8 nm band is dominated by an N or N^+ feature at low altitudes and that sub-limb measurements of the 61.6/87.8 brightness ratio follows $\Sigma O/N_2$, similar to the 135.6/LBH ratio. One conclusion of this work was that a retrieval of O and N_2 profiles from the ICON EUV measurements is plausibly feasible.[2]

This memorandum documents the development and validation of an algorithm to retrieve O and N_2 altitude profiles using ICON measurements of EUV dayglow. Section 2 provides a brief overview of the ICON EUV data. The forward model retrieval technique is described in Section 3, and the development

Manuscript approved February 21, 2023.

of the forward model is described in Section 4. The results and validation of the retrieval are discussed in Sections 5-7.

2. ICON EUV DATA

The ICON EUV instrument is a 1D imaging spectrometer. The raw output of the instrument is a 2D array of photon counts, with 108 pixels in the spatial (imaged) dimension aligned to local vertical spanning roughly 20-550 km tangent altitude, and 168 pixels in the spectral dimension spanning wavelengths 54-88 nm at 2.4 nm resolution. In order to accurately convert these measured photon counts into emission brightness (in units of Rayleighs), the instrument completes a monthly on-orbit absolute flux calibration via observations of the full moon, and a flat-fielding calibration obtained from a nadir-pointing measurement (see Sirk et al.[12]). The calibrated flux is summed across the emission feature as defined by empirically derived wavelength bins in order to generate the ICON EUV Level 1 (L1) data product, which reports limb profiles of emissions in twelve wavelength bands centered on specific, known EUV airglow emission features. In the ICON EUV data products, these color bands are named based on the brightest or central feature expected within the band, but in some cases the band can contain multiple spectrally-adjacent emission features.

Two of these wavelength bands are the 61.6 nm and 83.4 nm O^+ emissions which are used in the ICON daytime ionospheric retrieval. These are both primarily produced by ionization of O into an excited state of O^+, followed by naturally occurring decay into a lower-level state that generates an EUV photon. The 83.4 nm photons are resonantly scattered by ambient ionospheric O^+, so the shape of the measured altitude profile of the emission brightness contains information about the distribution of the F-region ionosphere. The 61.6 nm emission is optically thin to the ionosphere and can be used to characterize the original source function of 83.4 nm photons. The combination of these emissions thus allows for a retrieval of the peak height and density of the F-region ionosphere, which constitute the EUV Level 2 (L2) product [13, 14]. The ICON ionospheric algorithm scales its forward model of the 61.6 nm emission to define the airglow source but does not attempt to directly infer O from these emissions. However, the 61.6 nm emission ties directly to O densities, and in this work is used to infer O.

Of the remaining defined bands, five (labeled as 53.7 nm, 55.5 nm, 67.3 nm, 71.8 nm, and 79.1 nm) have been shown to be dominated by other O^+ features, of which all but one are dimmer than 61.6 nm. The 53.7 nm dayglow, while measured to be brighter than 61.6 nm, has a line center that is located off of the imaged region of the detector and thus does not contribute as much signal to the image as the other primary emissions of interest. Another, the bright 58.4 nm band, is dominated by a He line of the same wavelength, which is produced primarily by resonant scattering of solar photons. The 64.6 nm and 74.1 nm bands are dim and appear to have different altitude profiles compared to the O^+ features; these are likely blends of features with O and N_2 parents. The 76.7 nm band has not been identified but has been traced back most likely to be a reflection inside the instrument.

The final band at 87.8 nm has been shown to track with N_2 at low altitudes and is the other emission of interest to this work. The ratio of 61.6 nm to 87.8 nm correlates to the FUV ratio 135.6 nm to LBH sub-limb region (50-140 km) where the ICON EUV and FUV fields of view overlap. Tuminello et al. [2] speculated that these two EUV features could be used to measure thermospheric O and N_2. In the sections that follow, we will describe our creation of an EUV dayglow model which generates the emission profile of a chosen feature, and demonstrate how we use this model to characterize the different contributing emissions to the EUV 87.8 nm band, yielding a forward model which estimates the total emission profile in the ICON EUV

L1 87.8 nm band for a given atmospheric composition. We then use this forward model along with our model of the 61.6 nm emission band as the basis to conduct an iterative fitting to the altitude profiles of these emissions using discrete inverse theory with maximum likelihood to infer the underlying O and N_2 density profiles.

3. LIMB RETRIEVAL METHOD

In order to retrieve atmospheric densities from ICON EUV airglow profiles, we conduct a forward model inversion using discrete inverse theory (DIT). This is the same method used for the ICON EUV ionosphere retrieval algorithm [13] and has previously been used to retrieve altitude profiles of thermospheric neutral density composition using limb-profile measurements from TIMED-GUVI [4].

A forward model (**F**) predicts the value of observed quantities ($\vec{y}$) for given state parameters of a physical system ($\vec{x}$).

$$\vec{y} = \mathbf{F}\vec{x} \tag{1}$$

In this formalism, (**F**) is the airglow model which predicts the measured brightness altitude profile of an emission feature ($\vec{y}$) for given profiles of O, O_2, and N_2 density ($\vec{x}$).

Our consideration here is an inverse problem, where we wish to recover the atmospheric state from the airglow measurement. The forward model **F** is a non-linear operator, and the inverse of **F** is not well-defined (and is in our case under-determined). The DIT approach finds the parameters whose forward model image is the best fit to the measurement vector within the uncertainties represented for $\vec{y}$. To do so, the parameters of $\vec{x}$ are iteratively adjusted to improve the fit to $\vec{y}$ until converging to an optimized vector of parameters. This process involves repeated calls to the forward model to estimate the model Jacobian matrix via finite difference. Further details can be found in the works of Meier and Picone [15] and Picone et al.[16].

It is possible to implement the DIT algorithm using atmospheric densities on an altitude grid as the state vector $\vec{x}$; however this would create a large parameter space with large regions corresponding to physically unrealistic atmospheres. A high dimensionality of $\vec{x}$ would also render finite difference approximations of the Jacobian computationally expensive. Finally, any reasonably spaced density grid would correspond to a state vector with dimension around that of the measurement vector, meaning that DIT would return an under-determined solution. For these reasons, we use MSIS 00 as a driver to reduce the atmospheric state vector to three parameters. The first parameter is a scalar of the solar F10.7 input to MSIS 00. The second and third are scalars applied directly and uniformly to the MSIS 00 output O and N_2 density profiles, respectively. While our approach includes the capability to also scale the O_2 density profile, our early tests found this to have little impact on the measured altitude profiles because it only has relevance to photon absorption at the lowest altitudes below our region of interest, so this output remains unmodified other than by the changes to the F10.7 index. The rest of the MSIS 00 inputs, such as latitude, longitude, and A_p are also left unchanged, defined only by the conditions of each specific measured altitude profile. This effectively constitutes a catalog of physically reasonable atmospheres which may be slightly altered by changing only three parameters.

Figure 1 shows an example of a single retrieval. The top left plot shows the measured dayglow profiles and the initial forward model output. The three parameters are adjusted until they converge to the values seen in the text at the bottom right. The top right plot shows the forward model updated to the atmosphere given by the scaled parameters, and the O and N_2 densities associated with this atmosphere are shown in the solid lines in the bottom left panel.

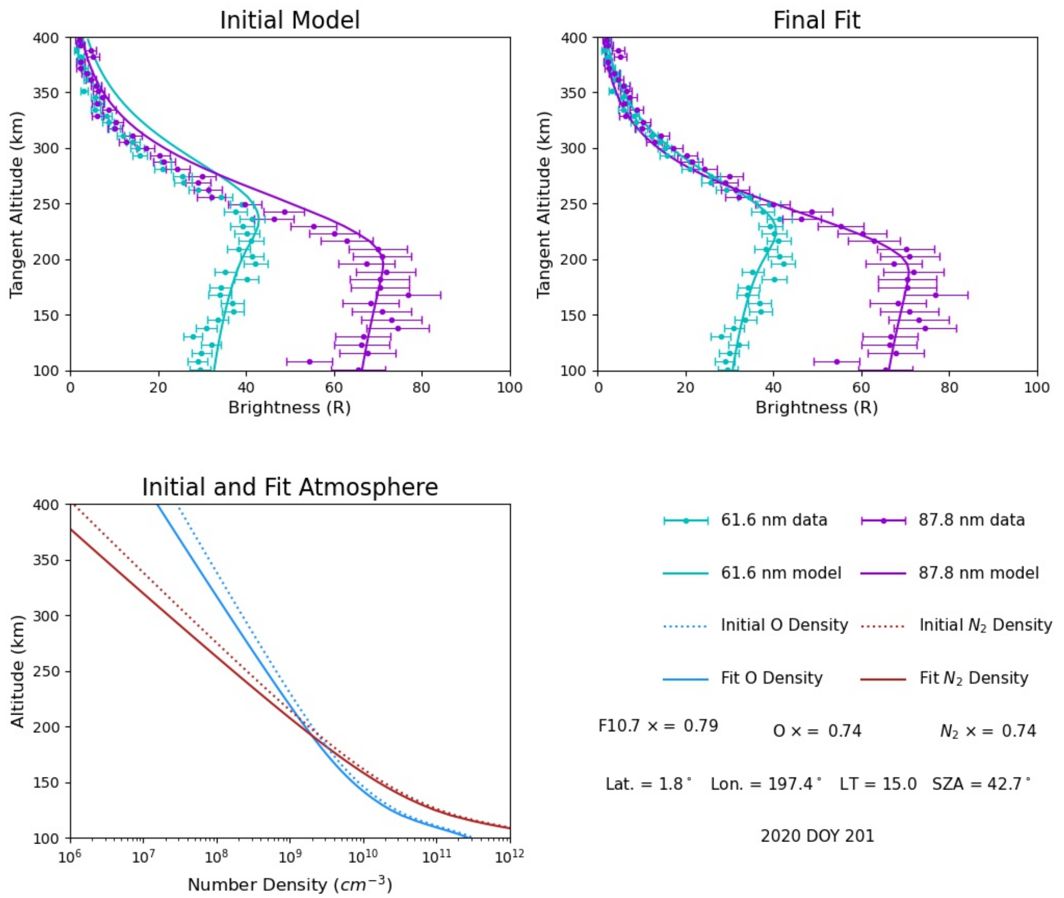

Fig. 1—A single forward model retrieval, showing the initial conditions and forward model output with the final fit and forward model output. The initial atmospheric state from scaled MSIS results in a peak that is too high, and the final fit shows that the peak has been lowered by decreasing the F10.7 input and scaling down O and N_2 densities.

4. THE EUV DAYGLOW MODEL

4.1 Model Architecture

Our DIT retrieval architecture requires a forward model that predicts dayglow profiles given the atmospheric state. The forward model must contain the underlying physics that produces the emissions, in this case the production of airglow by solar and photoelectron excitation and the transport of photons under absorption by neutrals. The geometry of the dayglow model is shown in Fig. 2.

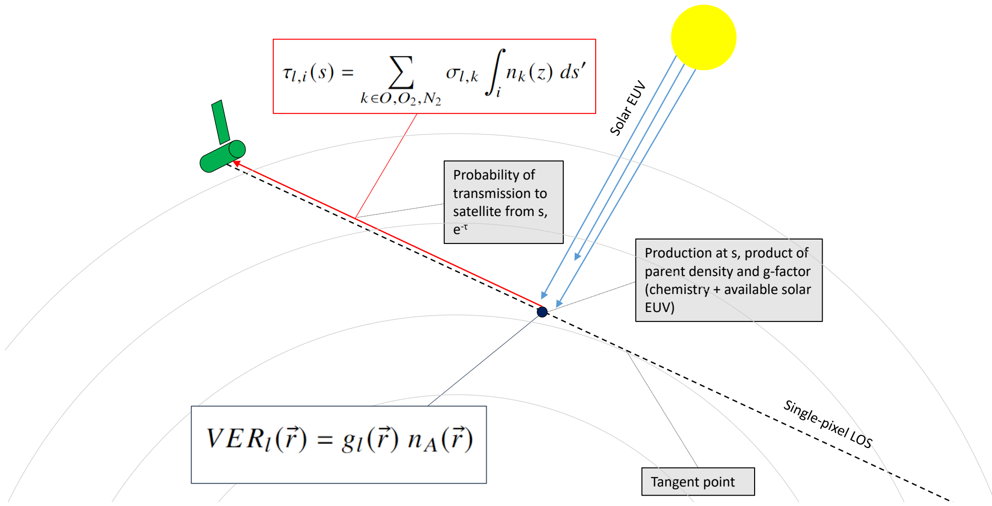

Fig. 2—Diagram of the forward model geometry. To find the contribution from a single point, the volume emission rate is calculated at that point (Eq. (2)), and the optical depth is found by integrating neutral density along the red path to the satellite (Eq. (7)). Another integration is performed to sum up these contributions along the entire line of sight (Eq. (6)).

4.1.1 Production

For a given airglow feature l with parent A, we express the volume emission rate (VER)

$$VER_l(\vec{r}) = g_l(\vec{r})\, n_A(\vec{r}) \tag{2}$$

where n_A is the number density of species A (assumed to vary only with altitude). It is important to note that this is the species prior to excitation. For example, 61.6 nm is created by an excited-state transition of O^+ ion but has a parent source of O that is ionized to the upper-level excited state. Equation (2) serves as the definition of the g-factor g_l , which contains both the photochemistry of A and the availability of the source of excitation (solar UV and photoelectrons). The solar component of the g-factor is given by:

$$g_{l,s}(\vec{r}) = \int_{\nu_0}^{\infty} \sigma_l(\nu)\, F(\vec{r}, \nu)\, \mathrm{d}\nu \tag{3}$$

where F is the attenuated solar flux of frequency ν at position $\vec{r}$, $\sigma_l(\nu)$ is the excitation cross section to the excited state that produces emission l, and ν_0 is the frequency corresponding to the excitation threshold.

The EUV emissions have a small contribution from photoelectron impact excitation, and the photoelectron g-factor follows a similar form:

$$g_{l,e}(\vec{r}) = \int_{E_0}^{\infty} \sigma_{l,e}(E)\, \Phi(\vec{r}, E)\, \mathrm{d}E \tag{4}$$

where $\Phi(\vec{r}, E)$ is the differential photoelectron flux at energy E at position $\vec{r}$, $\sigma_{l,e}(E)$ is the photoelectron excitation cross section, and E_0 is the excitation threshold energy. The g-factor is the sum of the solar and photoelectron contributions.

$$g_l(\vec{r}) = g_{l,s}(\vec{r}) + g_{l,e}(\vec{r}) \tag{5}$$

For the emissions under consideration for this work, the production is dominated by solar photoionization, with any photoelectron contribution being less than ~10% above 200 km.

Because we are evaluating emissions for which routine measurements have not been made, we have adapted g-factors for the well-characterized 83.4 nm and N^+ 108.5 nm emissions as our proxies for O and N_2 parent emission features, respectively. These g-factors are parameterized, based on runs of the Atmospheric Ultraviolet Radiance Integrated Code (AURIC)[17], as a function of solar zenith angle, solar F10.7 index, and column density. These g-factors must then be scaled to match the observed emission characteristics of the targeted model emission features (see Section 4.2).

4.1.2 Transport

The g-factors allow us to model the initial production of photons, but these photons will undergo absorption and scattering by the atmosphere as they pass from the location of production to the sensor. At these wavelengths, we assume that only absorption by neutrals is of concern based on the shapes of the profiles [2]. Under this assumption, the total brightness along a single line of sight j is given:

$$I_{l,j} = \int_j VER(z)\ e^{-\tau_{l,j}(s)} \mathrm{d}s \tag{6}$$

where $\tau_{l,j}(s)$ is the optical depth of feature l at point s along path j. We consider absorption by neutral O, O_2, and N_2. The optical depth is calculated:

$$\tau_{l,j}(s) = \sum_{k \in O, O_2, N_2} \sigma_{l,k} \int_j n_k(z)\ \mathrm{d}s' \tag{7}$$

where $\sigma_{l,k}$ is the cross-section for absorption of a photon at the wavelength of l by species k and the integral is evaluated between the point s and the spacecraft along line of sight j. Cross-sections for O have been measured at high resolution (Meier 2022, private communication) and for O_2 and N_2 have been taken from Conway [18]. The calculation is repeated for the line of sight j of each pixel to generate the modeled airglow profile.

4.1.3 Optimization

The dayglow model is called many times during the inversion, both to evaluate the fit of the atmosphere to the observations and to estimate the derivatives with respect to forward model parameters. Therefore, it is important that the model is computationally efficient. Each call to the forward model consists of a path integral (Eq. (7)) which is to be evaluated at each point of an outer integral (Eq. (6)) for each of the tens of pixels. We evaluated versions of the forward model that used straightforward implementations of numerical integration techniques (such as Newton-Cotes and Simpson's Rule) but these were found to be too slow for the inversions to be completed in a reasonable amount of time within our Python-based code structure.

We define an altitude grid vector of length m and $m \times n$ matrix $\mathbf{\Pi}$, where the n is the number of spatial pixels (defined by the altitude of the tangent point) being modeled. The element Π_{ij} is the distance along line of sight j from the satellite to the altitude of grid point i:

$$\Pi_{ij} = \int_{z=z_{sat}}^{z=z_i} \mathrm{d}s = \sqrt{r_s^2 - r_{0,j}^2} - \sqrt{r_l^2 - r_{0,j}^2} \tag{8}$$

where r_s is the radial distance from the Earth's center (from here, *radial height*) to the satellite, $r_{0,j}$ the radial height of tangent point j, and r_l the greater of $r_{0,j}$ and the radial height of grid point i, r_i. We then define the $m \times n$ matrix $\mathbf{\Delta}$ where:

$$\Delta_{ij} = \begin{cases} \Pi_{ij} - \Pi_{(i+1)j} & i < m \\ \Pi_{ij} & i = m \end{cases} \tag{9}$$

Let $\vec{q}$ be a vector of length m such that $q_i = q(z_i)$, the value of some quantity (e.g. number density) at the altitude grid point z_i. Then the integral along line of sight j between grid points u and v is

$$\int_{z=z_u}^{z=z_v} q(z)\, ds \approx \sum_{i=u}^{v} \Delta_{ij}\, q_i \tag{10}$$

under the rectangle rule. Finally, we let $\mathbf{Q}$ be an $m \times n$ matrix where each column is $\vec{q}$ and calculate the matrix $\mathbf{Y}$.

$$Y_{ij} = \sum_{k=i}^{m} Q_{kj}\, \Delta_{kj} \tag{11}$$

The elements of matrix $\mathbf{Y}$ are the line integral along path j from the satellite to grid point i for each gridpoint and line of sight, each of which would have been individually calculated when finding the optical depth, for example.

The approximation in Eq. (10) is poor compared to more refined means of sampled integration, but the error becomes small for high resolution altitude grids since the quantities integrated are well-behaved. We use a grid at 0.5 km resolution from 100 km to 400 km and 1.0 km resolution from 400 km to 590 km (the satellite altitude), which yields profiles that are nearly identical (well within data uncertainty) at significantly higher performance. Furthermore, $\mathbf{\Delta}$ is constant for a given viewing geometry. It is calculated once per ICON exposure and may be reused for subsequent calls to the forward model while DIT finds the best fitting model parameters.

4.2 Modeling the 87.8 nm Band

In order for the dayglow model to accurately predict EUV instrument response for given neutral density profiles and observation conditions, the airglow features composing each bin must be well-characterized. The 87.8 nm band on the ICON EUV instrument has previously been shown to track with N_2 at low altitudes.[2] The nominal 84.5-87.2 nm range of this bin contains several N and N^+ features [19] that are assumed to be generated by the photodissociative excitation of N_2, and the nearby 87.8 nm O doublet has previously been observed in the limb dayglow[20]. In this section, we show that the 87.8 nm band is comprised of a blend of these O and N features and describe the process by which we determine the contribution of each.

Recall (see Section 4.1.1) that our available g-factors are for production of O^+ 83.4 nm and N^+ 108.5 nm dayglow derived from O and N_2, respectively. We make a simplifying assumption and model the g-factors of the lesser-studied features of interest as scalar multiples of the well-tested 83.4 nm (O parent) or 108.5 nm (N_2 parent) g-factors. This approach has previously been used to model the 61.6 nm O^+ emission for

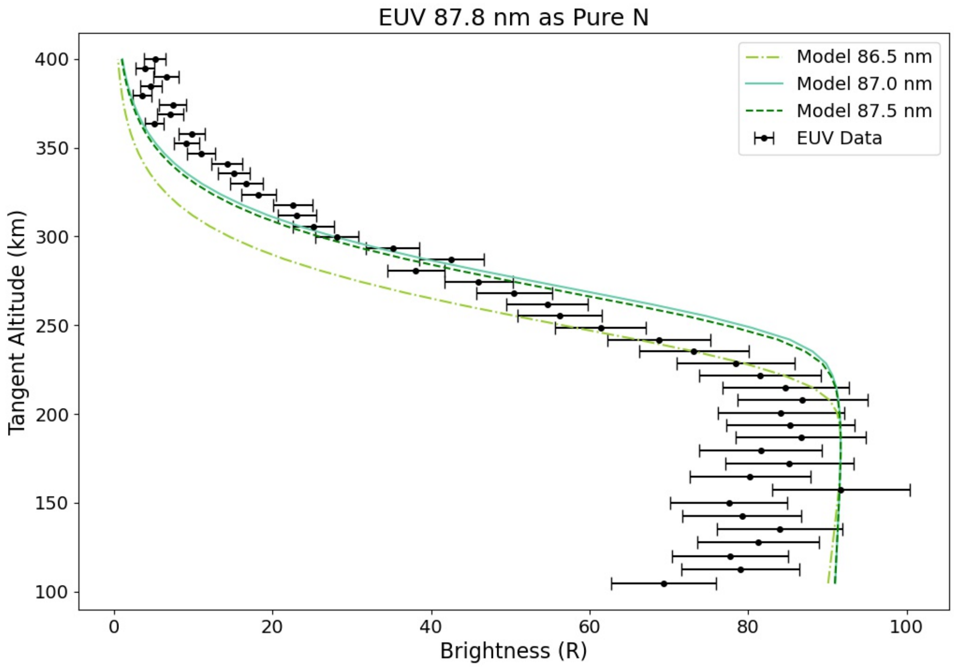

Fig. 3—An example of an ICON EUV 87.8 nm exposure (black) compared to forward model output of three *N* features (green).

the ICON EUV ionosphere retrieval [13]. To correctly model a given feature or blend of features, we must determine the appropriate scaling of the O^+ 83.4 nm and/or N^+ 108.5 nm g-factors.

To accomplish this, we first fit the ICON EUV L1 data collected over the entirety of year 2020, keeping the neutral density profiles fixed but adjusting the blending and scaling of the contributing emission features within the band. Under this scheme, we assume that MSIS 00 is climatologically correct. However, previous work showed that MSIS O and N_2 densities should be scaled by ~85% for low solar conditions [4, 21], as is the case for all of 2020 - therefore, we have completed this precursory part of the analysis using the MSIS outputs for O and N_2 scaled by this amount.

Initially, we attempted to model the 87.8 nm band as a pure N feature, with a scaled N^+ 108.5 nm g-factor and absorption cross-sections at a single wavelength. Figure 3 shows the forward model output of three candidate features with absorption cross-sections at 86.5, 87.0, and 87.5 nm. The forward model is linear in scaling of the g-factor, so each curve has been normalized to peak at the same brightness so that we can compare the shape of the profiles. All three fail to reproduce the modest peak around 200 km and the topside emission scale height of the measured 87.8 nm profiles. Modeling the band as a blend of these features also fails to reproduce the shape seen in the data.

Figure 4 shows the same ICON EUV profile as in Fig. 3, with a linear fit of the forward model output of the N 86.5 nm triplet and the O 87.8 nm doublet [19]. The blend of O and N features matches the shape of the profile above the peak and replicates the decreasing brightness below the peak. The O 87.8 nm has previously been observed in the limb dayglow [20], so we conclude that the EUV 87.8 nm bin is in

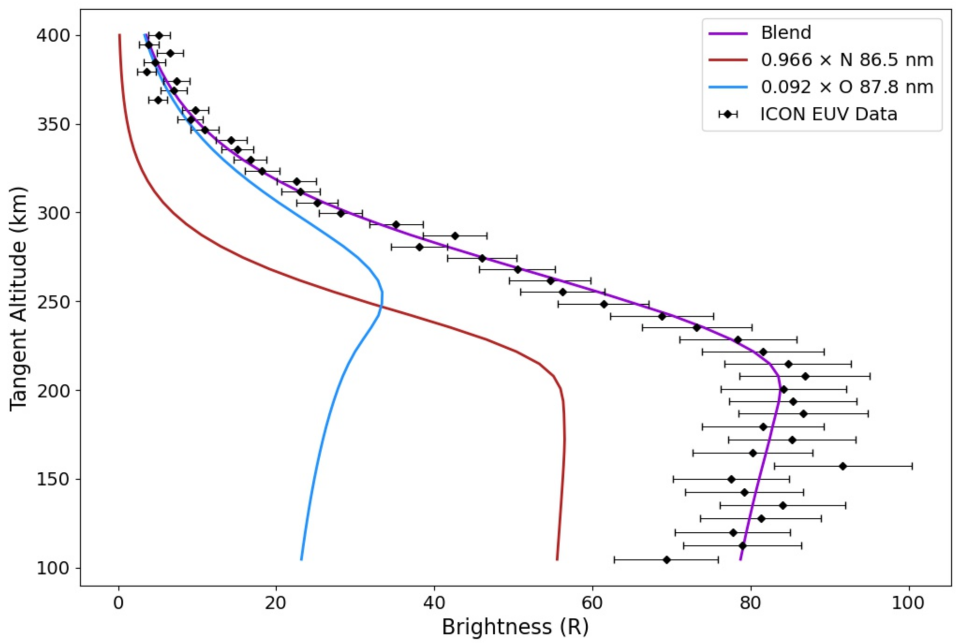

Fig. 4—An example of an ICON EUV 87.8 nm exposure (black) compared to a fit (purple) blending the N 86.5 nm triplet (red) with the O 87.8 nm doublet (blue). The legend indicates the factors by which the N^+ 108.5 nm and O^+ 83.4 g-factors are scaled, respectively. The shape of the data is well-modeled, though the data appear to be more noisy at low tangent altitude (see Section 4.3.2).

fact seeing this emission in addition to the previously documented N emissions. As for the N, it is likely that the instrument is seeing contributions from several N and/or N^+ features. The profiles are distinct, as the absorption cross-sections differ, but they are too similar for the fitting algorithm to consistently find a plausible fit using contributions at multiple wavelengths. Modeling of the EUV 87.8 nm bin could likely be improved by a detailed study of high resolution spectra, but for the purposes of this analysis, we consider the band to be comprised of O 87.8 nm and N 86.5 nm, since this line results in the best fits to the data.

In order to determine the appropriate scaling of the O^+ 83.4 nm and N^+ 108.5 nm g-factors (and thus the blending of respective 87.8 nm and 86.5 nm features), we have conducted a survey over every fifth day of ICON EUV data throughout 2020. To improve signal-to-noise ratio (SNR) in these dim emissions, we sum up five consecutive 12-second ICON EUV exposures to create an effective 60 second exposure. Using the observation conditions (local time (LT), latitude, longitude, and solar zenith angle (SZA)) of the middle exposure and central spatial pixel and a scaled MSIS atmosphere, we run the dayglow model for O 87.8 nm and N 86.5 nm and use DIT (see Section 3) to find the g-factor scalars which produce the best fit to the EUV data. Figure 4 depicts an example of this.

The median value of the g-factor scalars from the fits are 0.794 and 0.0708 for the 86.5 nm and 87.8 nm features, respectively. Figure 5 shows the distribution of these scalars normalized by dividing by the median value. The deviation of actual atmospheric profiles from MSIS climatology is one known cause of the spread in these distributions. Another possible source is that scaling the g-factors from another emission

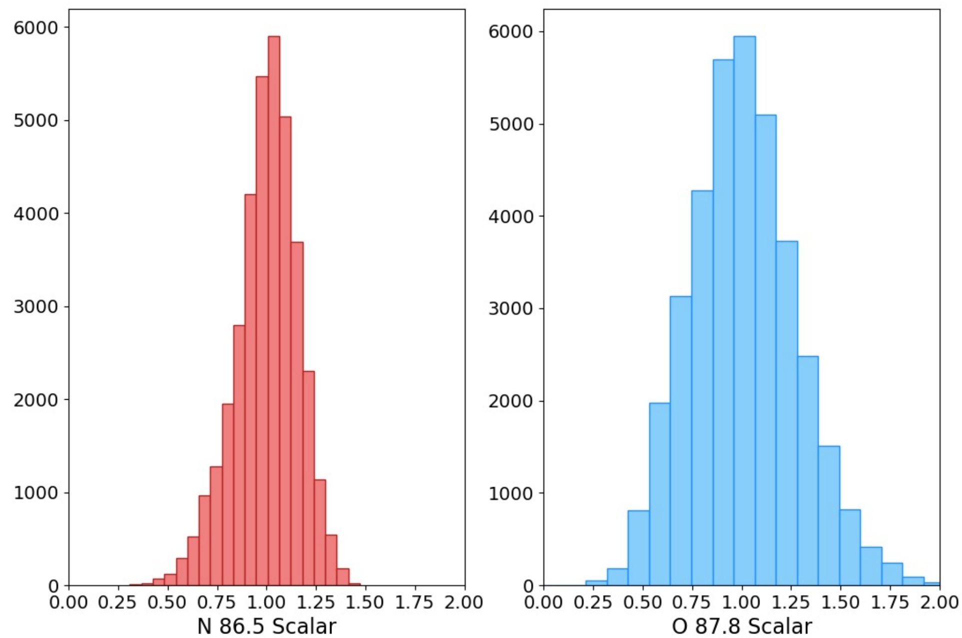

Fig. 5—Histograms indicating the distribution of the normalized g-factor scaling for the 86.5 nm and 87.8 nm features over the course of 2020.

only provides an approximation of the g-factors of the desired emission, since the photochemistry differs between the atomic transitions. The most obvious difference between these emission features and the O^+ 83.4 nm and N^+ 108.5 nm features is that the energies of solar EUV photons that create these states will have different cut-offs, as well as different corresponding atmospheric attenuation. While the distribution of the scalars around a central value supports the approach we have used, this scaling remains as a potential source of systematic uncertainty within the density retrieval algorithm.

As shown in Figs. 6 – 7, the g-factor scalars vary with local time and (to a lesser extent) throughout the year. Once again, this is likely caused in part because MSIS does not exactly characterize the short-term variation of the atmosphere with local time, season, or solar conditions; or it could be that the g-factor scaling approximation varies in accuracy with atmospheric and solar conditions. It is likely a combination of both. It is also worth noting that some of the variation at early and late LT could be due to more complicated solar geometry at high solar zenith angles.

Local time and coverage cycle are the best predictors of the optimal g-factor scalar, so the data shown in Figs. 6 – 7 are median-averaged by LT bin for each coverage cycle and interpolated to create a lookup table like the one shown in Fig. 8. For each ICON exposure, the forward model uses these tables to determine the scaling of the 83.4 nm and 108.5 nm g-factors.

4.3 Modeling the 61.6 nm Band

The ICON EUV sensor was designed such that the 61.6 nm band would spectrally isolate the O^+ 61.6 nm triplet [12], as this feature is a measurement requirement for the ICON daytime ionosphere retrieval [13].

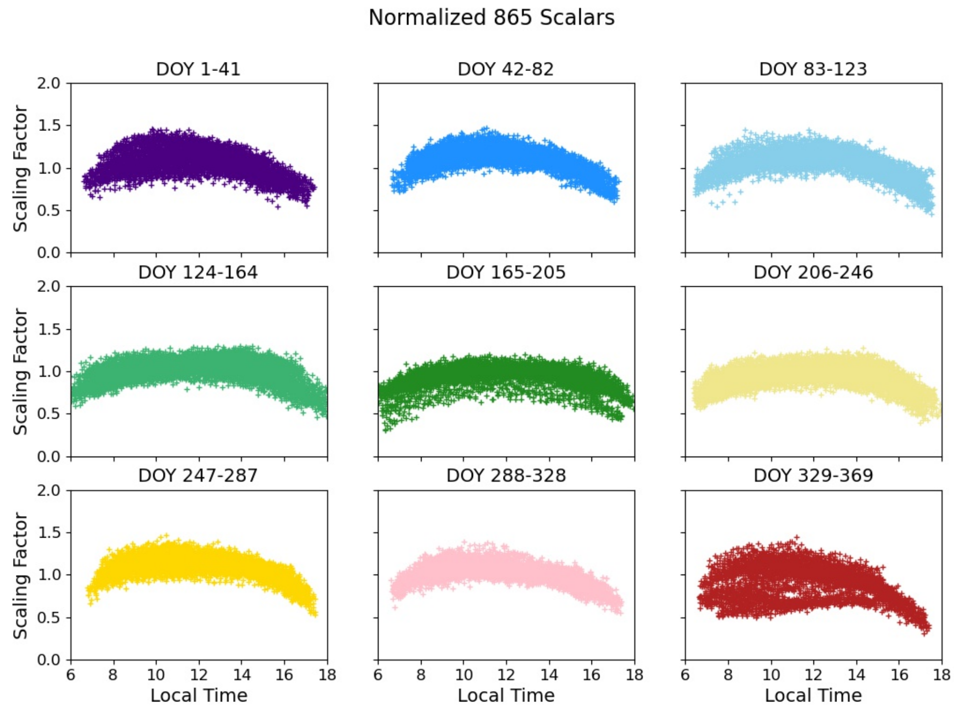

Fig. 6—Normalized g-factor scaling for the *N* 86.5 nm feature vs local time, broken down by ICON coverage cycle.

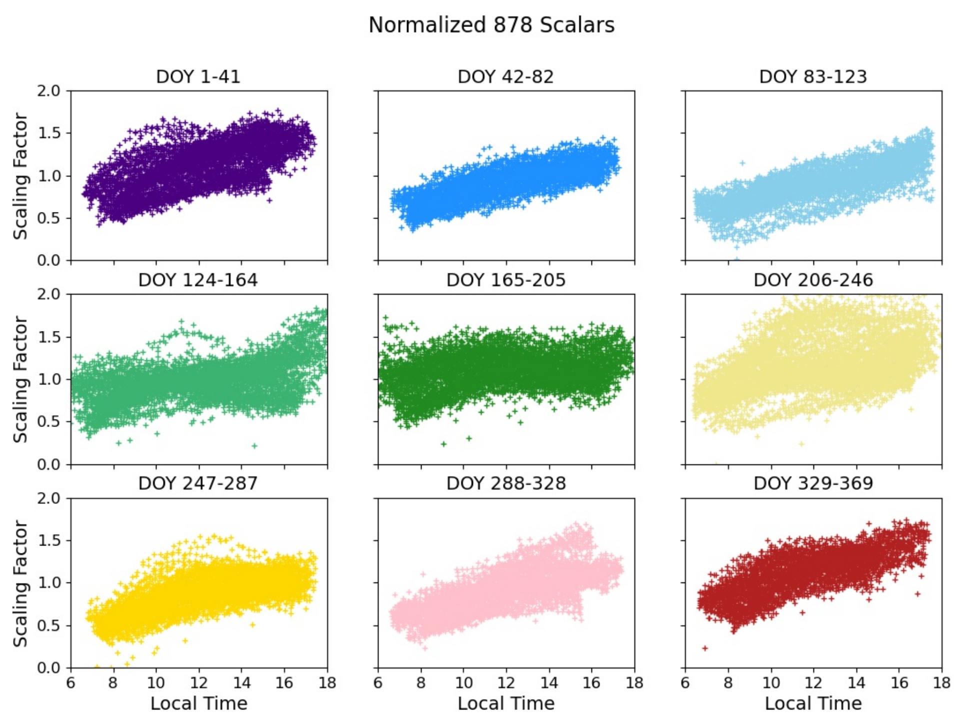

Fig. 7—Normalized g-factor scaling for the *O* 87.8 nm feature vs local time, broken down by ICON coverage cycle.

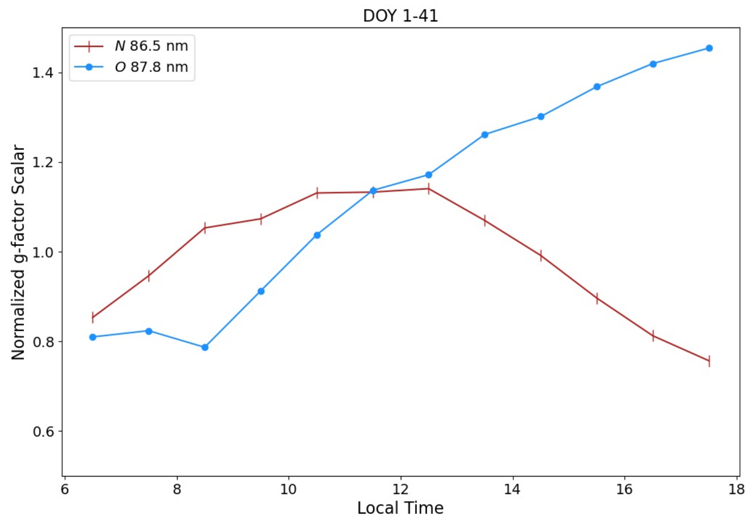

Fig. 8—Lookup table for the 86.5 nm and 87.8 nm g-factors for DOY 1-41.

We use a similar method here to determine the 83.4 nm g-factor scaling factor to be applied for the O^+ 61.6 nm emission. The EUV 61.6 nm data is well reproduced by our airglow model using this single O^+ feature, which is evidence that the design works as intended. However, both our airglow model and the forward model used in the EUV ionosphere retrieval show disagreement from the data at high tangent altitude. In Section 4.3.1, we describe the process for determination of the appropriate g-factor scaling for the 61.6 nm feature, and in Section 4.3.2, we derive and discuss the application of a correction for the 61.6 nm data to generate a better match to the model at high altitude.

4.3.1 Determining 61.6 nm g-factor Scaling

As for the 87.8 nm band (see Section 4.2) we conduct a survey over every fifth day of 2020. For each 60 second exposure, we run the airglow model for 61.6 nm on the (scaled) MSIS densities as before and find the scaling for the 83.4 nm g-factor that best fits the 61.6 nm data.

The median value of the 61.6 nm g-factor scalar over the whole dataset is 0.125. Figure 9 shows the distribution of the normalized g-factor scalars. The distribution of the 61.6 nm g-factor scalars is tighter than that of the 87.8 nm scalars (Fig. 5). This is largely because the blending of features in the latter is an additional source of systematic uncertainty as an error in the estimation of the scalar for one feature is coupled to the other. Our value derived here is also consistent with the value used within the ICON EUV daytime ionosphere algorithm.

There appears to be a secondary population in the right tail of the histogram in Fig. 9. Unlike the 87.8 nm scalars, these 61.6 nm scalars do not show a strong dependence on LT but rather show an increase near the end of 2020. This coincides with an increase in solar F10.7 index; however, the exact cause has not been confirmed at this time.

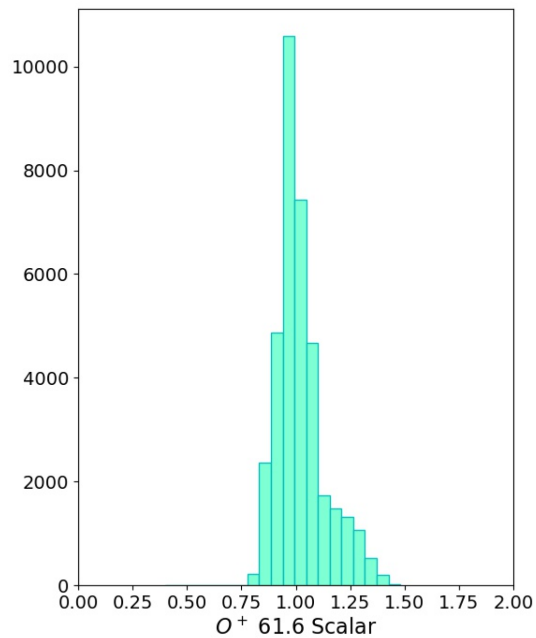

Fig. 9—Histogram indicating the distribution of the normalized g-factor scaling for the O^+ 61.6 feature over the course of 2020.

4.3.2 An Alternate Modeling: Corrections to the 61.6 nm Data

In Fig. 1, one can see that the initial run of the 61.6 nm forward model departs from the ICON EUV measurements near and above 300 km. This is not an isolated event but is instead representative of a trend: the ICON 61.6 nm measurements are generally dimmer than the model at high altitude. This is also the case for the 61.6 nm forward model used for the ICON EUV O^+ retrieval, indicating that there is plausibly some error in the measurements or in the g-factors, which are shared between the two models. This led us to experiment with "correcting" the 61.6 nm data in order to have data that (in the aggregate) more closely matched with the forward model under the scaled MSIS 00 atmosphere.

In order to determine the best means of correction, we examined how the measurements differed from the MSIS 00 driven forward model for a string of days from May 30 - June 24, 2020. We examined the disparity in both pixel and tangent altitude space, and we also considered the difference in brightness both absolute and relative to the forward model. Figure 10 shows the disparity relative to the forward model in pixel space, which we found to best characterize the trend. One reason for this is that at low pixel number (corresponding to low altitude), there is noticeable pixel-to-pixel variation that is consistent across days. At high altitudes, the aforementioned trend is shown, where the forward model is brighter at higher altitudes, more-so than at middle and low altitudes.

In order to correct for this bias at high altitudes, we calculate the value of the relative disparity at each pixel ρ_i (the quantity shown in Fig. 10) for a given day and apply a correction as follows:

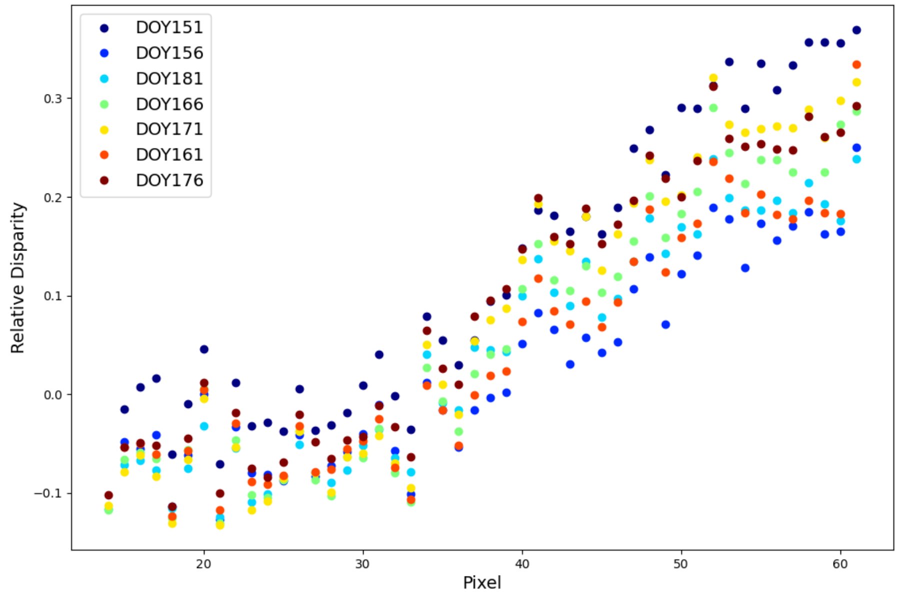

Fig. 10—Median disparity between the measured and modeled 61.6 nm radiance at the pixel indicated on the abscissa. The disparity is of the form (model-measurement)/model, so that a positive value is indicative of the model being brighter than the measurement.

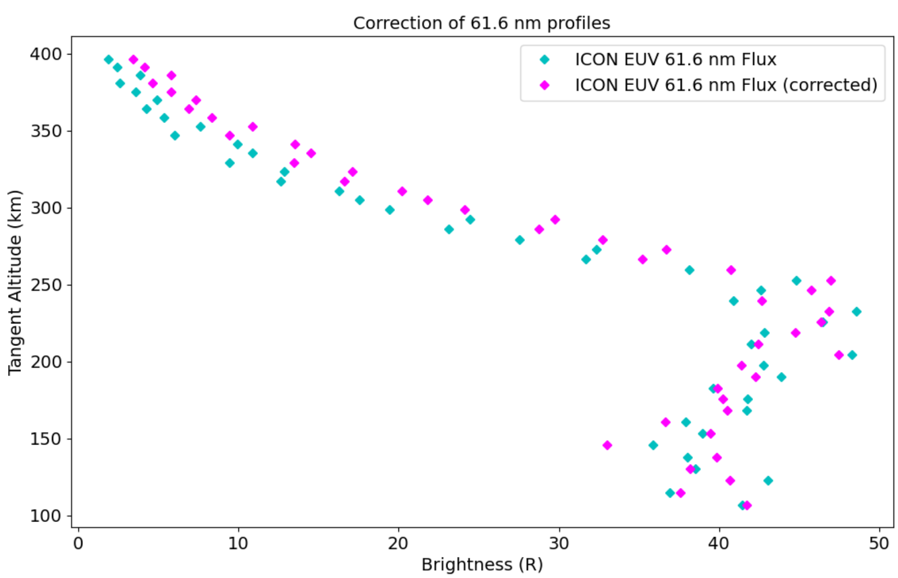

Fig. 11—A measured (blue) 61.6 nm profile that has been corrected (pink) with the procedure described in Section 4.3.2.

$$y_i' = y_i + \rho_i\,(\mathbf{F}x)_i \tag{12}$$

where y_i is the original measurement and $(\mathbf{F}x)_i$ the value of the forward model under scaled MSIS 00. This results in a corrected profile, an example of which is shown in Fig. 11.

Both in the interest of creating the highest quality atmospheric retrieval and to test the hypothesis that the 61.6 nm are artificially dim relative to the forward model at high altitudes, we have utilized an alternate retrieval which applies this correction to the 61.6 nm data before performing the inversion. Unfortunately, this cannot easily distinguish artificial dimming of the measurements through calibration error from artificial brightening of the forward model via bias in the g-factor; however, it should provide some indication of whether the discrepancy is best explained by one of the two factors or by a flaw in the assumption that scaled MSIS 00 can be assumed to be a correct climatology.

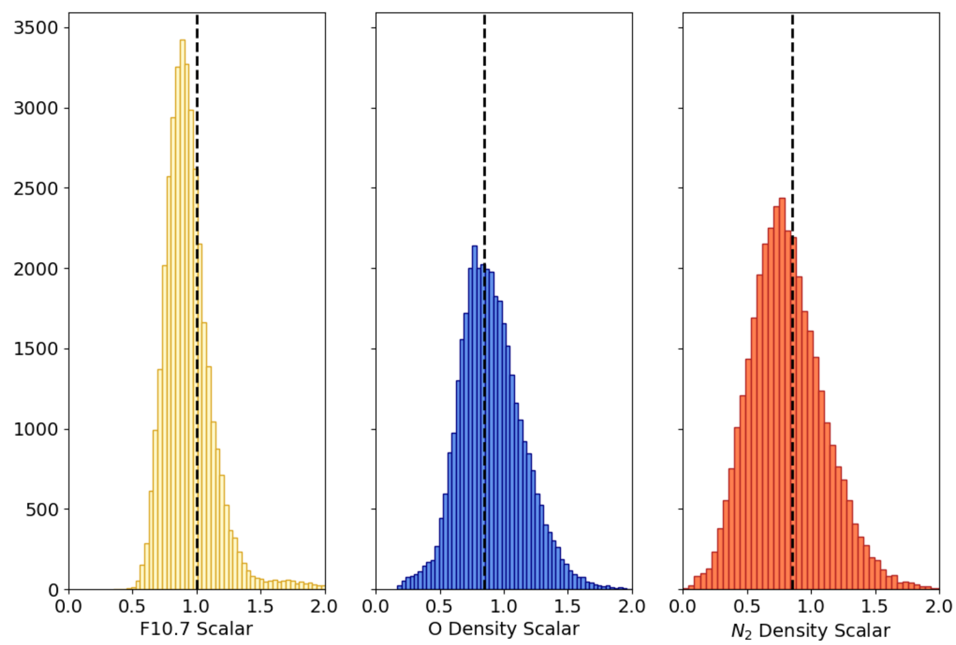

Fig. 12—Distribution of F107, O, and N_2 scalars for all retrievals in 2020. The dotted line indicates the initial value, 1.0 for F10.7 and 0.85 for the density scalars. (These values of 1.0 and 0.85 are respectively used in order to determine the g-factors.)

5. RETRIEVAL RESULTS

We ran the EUV neutral density inversion algorithm for all measurements between 6 and 18 LT during every fifth day of 2020, summing five consecutive ICON EUV exposures, now fixing the blending and scaling factors and iterating on our three density-relevant model parameters (see Section 3). Figure 12 shows the distribution of F10.7, O density, and N_2 density scaling factors from all retrievals. The distribution of

F10.7 scalars peaks below 1.0, indicating that the retrieval generally fits a cooler atmosphere to the EUV measurements compared to MSIS climatology. While the O scalar peaks around the training value of 0.85, indicating that the retrieval primarily adjusts O profile shape rather than scale (via F10.7), the N_2 scalar peaks lower, indicating that the shape and scale of N_2 profiles are adjusted.

5.1 Comparison to MSIS 00 Densities

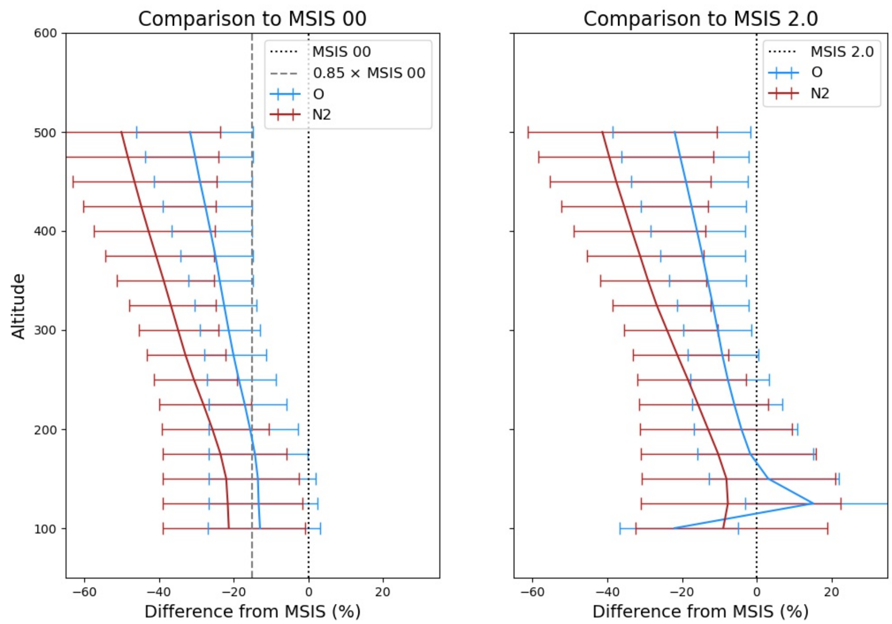

Fig. 13—The median difference (%) between the retrievals and MSIS 00 (left) and MSIS 2.0 (right). Error bars represent the upper and lower quartiles. The MSIS 00 plot indicates 85% of the MSIS 00 O and N_2 density, which are the values used to determine the g-factor scaling. The sharp peak in the O difference from MSIS 2.0 at 125 km is due to a change in the shape of the O density profiles between MSIS 00 and MSIS 2.0.

MSIS 00 is used for the driver of the model and was used to determine the g-factor scalars used in the forward model. Thus, comparison to MSIS 00 does not provide validation. However, the trends in differences between the retrieval and MSIS 00 indicate overarching results of the retrieval. For each EUV measurement, the MSIS 00 output with the initial scalars (1.0 for F10.7 and 0.85 for the densities), which we will compare to the retrieved densities which use the post-fit scalars.

The left pane of Fig. 13 shows how retrieved O and N_2 densities differ from MSIS 00 as a function of altitude. In the case of each species, the scale height is smaller above 200 km, which is why both densities are increasingly lower than MSIS 00 at high altitudes. The low altitude data show that the retrieved O density agrees with the scaled down MSIS 00, while the retrieved N_2 base is generally lower. These observations are in agreement with our interpretation of the scalar distributions in Fig. 12.

Figure 14 and Fig. 15 show retrieved and scaled MSIS 00 O and N_2 density (respectively) at 250 km altitude vs latitude and local time for a single ICON coverage cycle. Both plots show that the retrievals follow the seasonal trend, in this case northern hemisphere winter. However, while the retrieved O densities vary

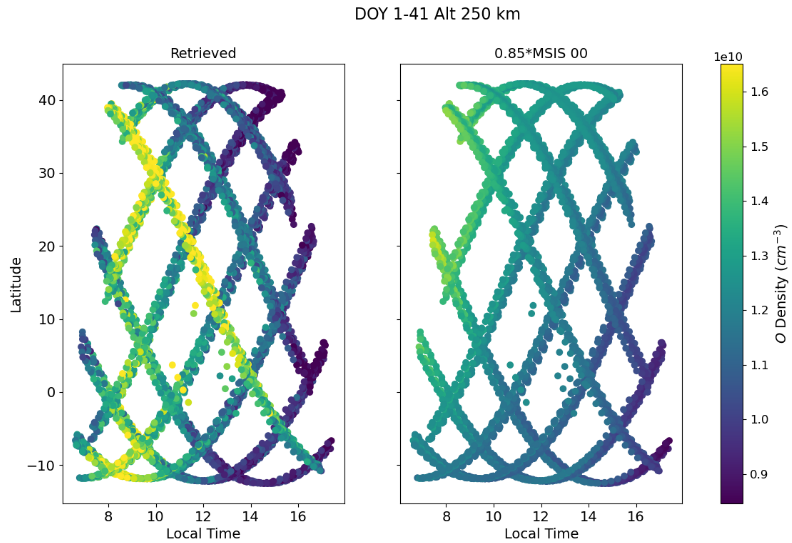

Fig. 14—EUV retrieved and scaled MSIS 00 O density from 2020 DOY 1-41 at 250 km altitude on latitude-LT map. The scale of O variation is comparable to that seen in MSIS.

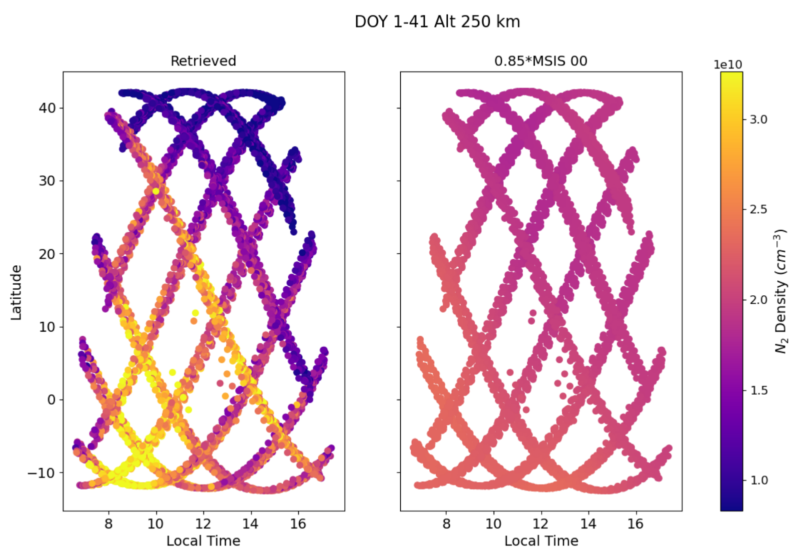

Fig. 15—EUV retrieved and scaled MSIS 00 N_2 density from 2020 DOY 1-41 at 250 km altitude on latitude-LT map. The retrieved N_2 density shows more extreme variation than that seen in MSIS.

on a similar scale to what is seen in MSIS 00, the retrieved N_2 densities show much more extreme variation. It is expected that measurements will show weather-like variation, which will result in a larger range of densities than what will be predicted by a climatological model like MSIS. The O densities are a plausible example of this, but the factor of roughly 3 between the lowest and highest N_2 density measurements is likely not explained by the same mechanism. Either MSIS 00 shows too little variation in N_2 density, or the EUV retrieval identifies too much.

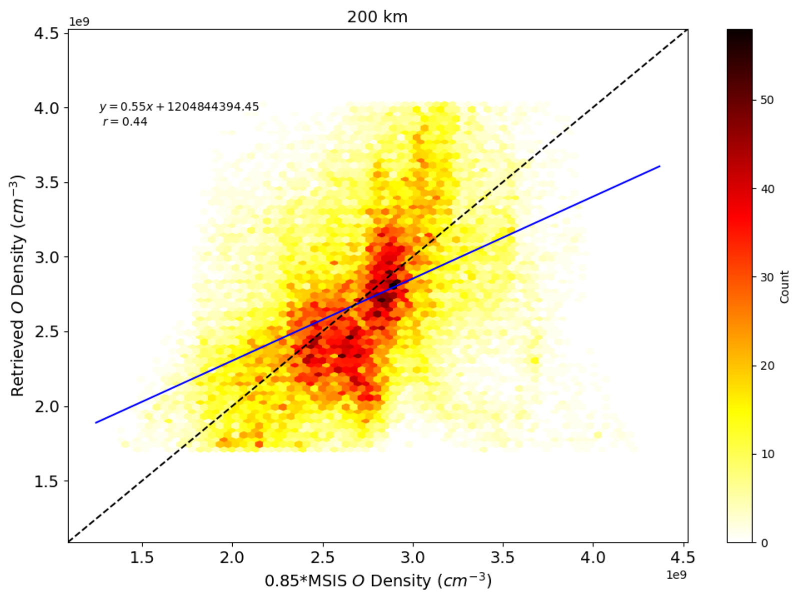

Fig. 16—Scatter density plot of retrieved and scaled MSIS 00 O density at 200 km. Retrieved densities lower than the 5th and above the 95th percentiles have been excluded. The dashed black line indicates unity, while the solid blue line is a least-squares with parameters indicated in the top-left.

Figures 16-19 show scatter density plots of retrieved and scaled (85%) MSIS 00 O and N_2 density at 200 and 300 km. These altitudes are just below the 87.8 nm peak and comfortably above both emission peaks, respectively. The data show lower correlation at lower altitude, where the retrieval is more absorption-driven. Absorption cross-sections are a major source of uncertainty, so it is of little surprise that this affects the retrieval. Also visible in Fig. 17 is the large range of N_2 densities compared to the range of MSIS 00 values. Upon examination, the least-squares fits in these plots are to be interpreted with caution as they seem to be overly influenced by measurements outside of the main population.

At 300 km, where the retrieval is more production-driven, the retrieved values correlate more strongly with MSIS 00, and the range of values observed in both species is more in line with that seen in MSIS. This also corresponds with a more characteristic least-squares fit for each species. In both O and N_2, the slope of the fit is below unity. If the retrieval is to be believed, MSIS 00 is systematically overestimating the change in density between observation conditions. Alternatively, the retrieval is under-sensitive to changes in density at these altitudes.

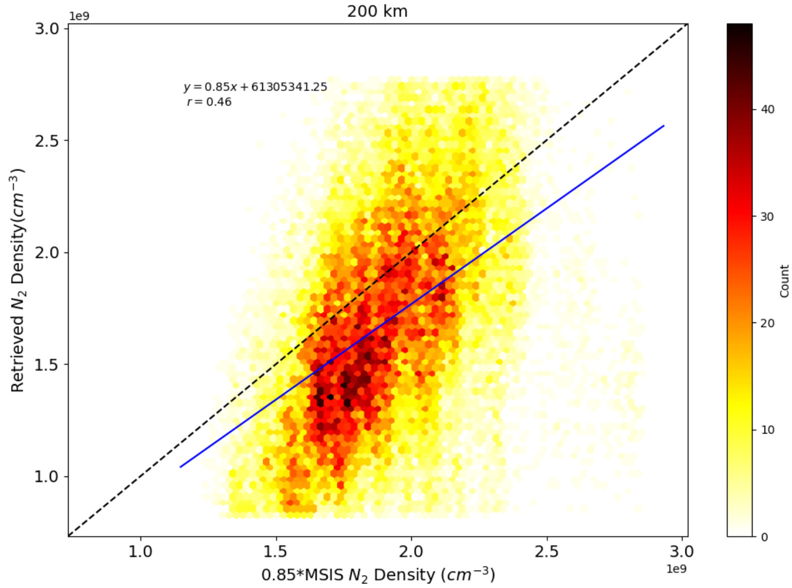

Fig. 17—Scatter density plot of retrieved and scaled MSIS 00 N_2 density at 200 km. Retrieved densities lower than the 5th and above the 95th percentiles have been excluded. The dashed black line indicates unity, while the solid blue line is a least-squares with parameters indicated in the top-left. The range of retrieved values noticeably exceeds the range of modeled values.

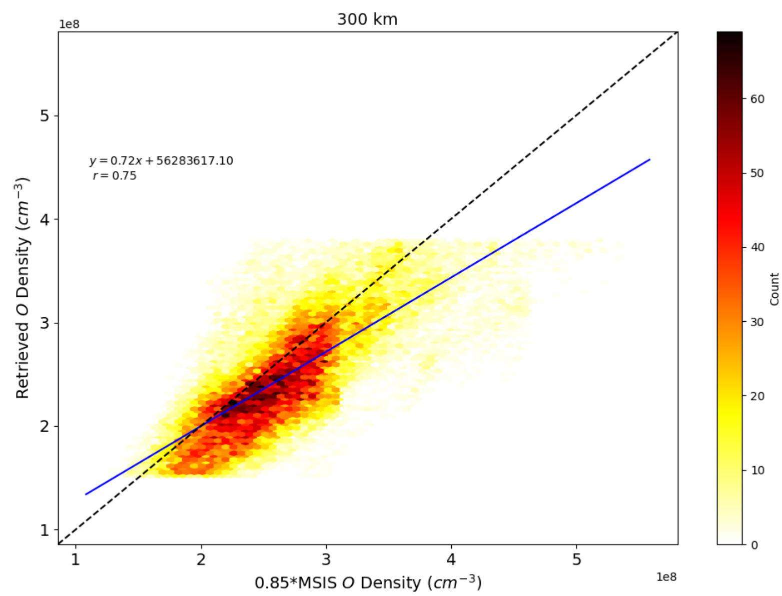

Fig. 18—Scatter density plot of retrieved and scaled MSIS 00 O density at 300 km. Retrieved densities lower than the 5th and above the 95th percentiles have been excluded. The dashed black line indicates unity, while the solid blue line is a least-squares with parameters indicated in the top-left. The fit has a slope less than unity, but it does appear to be affected by outliers at high modeled densities.

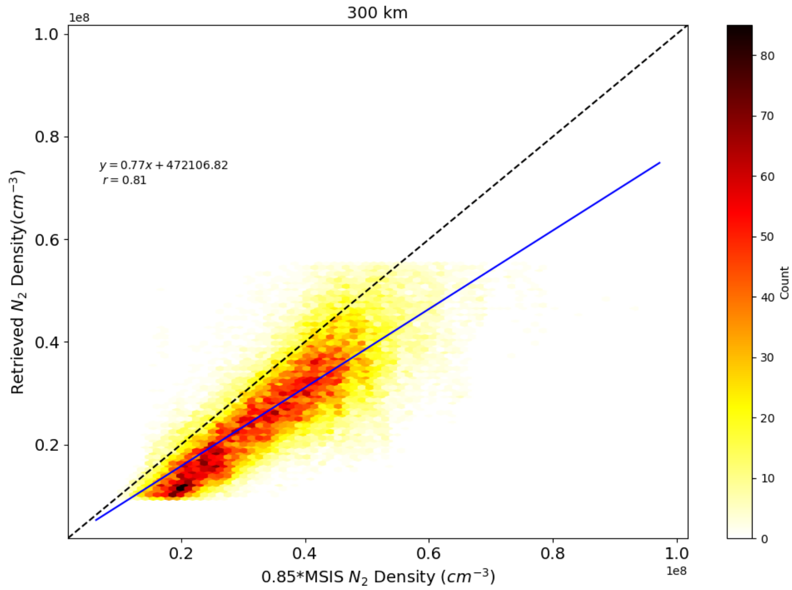

Fig. 19—Scatter density plot of retrieved and scaled MSIS 00 O density at 300 km. Retrieved densities lower than the 5th and above the 95th percentiles have been excluded. The dashed black line indicates unity, while the solid blue line is a least-squares with parameters indicated in the top-left. The range retrieved and modeled densities is comparable, in contrast to what is seen in Fig. 17

6. RETRIEVAL VALIDATION

The Gaussian-like distribution of the retrieved scalars is an indicator that the retrieval is physical, but this alone does not validate the EUV retrieval results. In this section, we qualify and provide validation for the EUV results by comparing to MSIS 2.0, SWARM accelerometer-derived mass density, and ICON FUV and GOLD O/N_2.

6.1 MSIS 2.0

While MSIS 2.0 is not an entirely independent model from the MSIS 00 model used to drive the retrieval, there is still information to be gained by comparing EUV retrieval measurements to MSIS 2.0. Namely, MSIS 2.0 has incorporated new data and is expected to be a major upgrade to MSIS 00. [3] Figure 20 shows the median difference in density profiles between MSIS 00 and MSIS 2.0 for the viewing conditions of all EUV retrievals. Immediately noticeable is a change in the shape of the O density profiles at low altitude. This change looks extreme in Fig. 20, but this is the result of a reasonable change in the inflection point of O density above the turbopause.

A qualitative interpretation of the scalar distribution in Fig. 12 and the left panel of Fig. 13 is that the retrieval has identified that N_2 needs to be scaled down by more than O does. Figure 20 shows that this is a change that was made in MSIS 2.0. However, MSIS 2.0 has N_2 decreased by about the assumed 15%, while reducing O by only 10%.

Figures 21-24 show scatter density plots of retrieved and MSIS 2.0 O and N_2 density at 200 and 300 km, similar to the plots shown in Section 5.1. The retrieved O density correlates with the MSIS 2.0 values

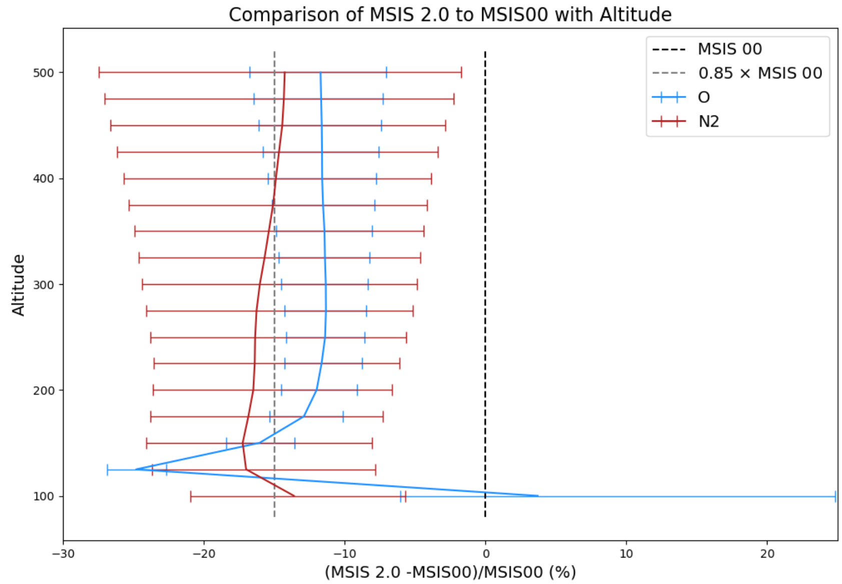

Fig. 20—Percent difference in O and N_2 density between MSIS 00 and MSIS 2.0. Error bars represent the upper and lower quartiles. The black dashed line represents equality, while the gray dashed line indicates 85% of MSIS 00 density, which was used to determine the g-factor scalars.

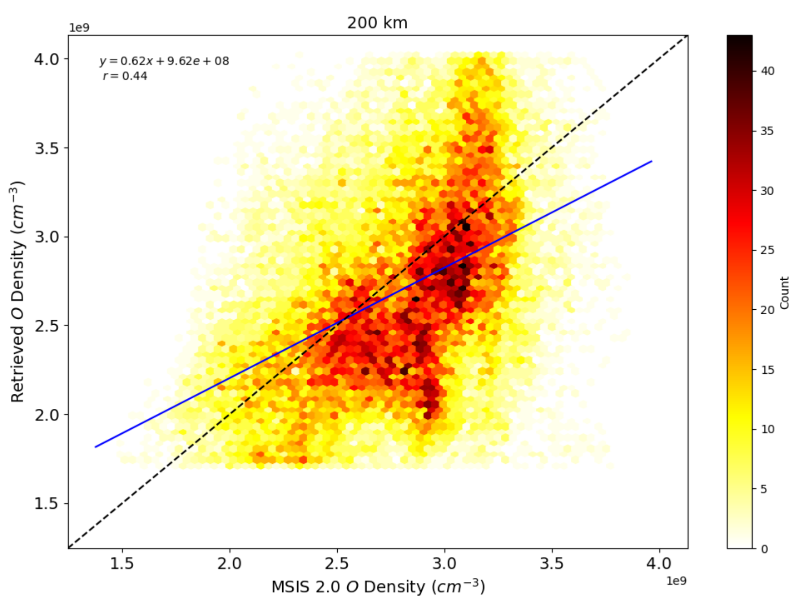

Fig. 21—Scatter density plot of retrieved and scaled MSIS 2.0 O density at 200 km. Retrieved densities lower than the 5th and above the 95th percentiles have been excluded. The dashed black line indicates unity, while the solid blue line is a least-squares with parameters indicated in the top-left.

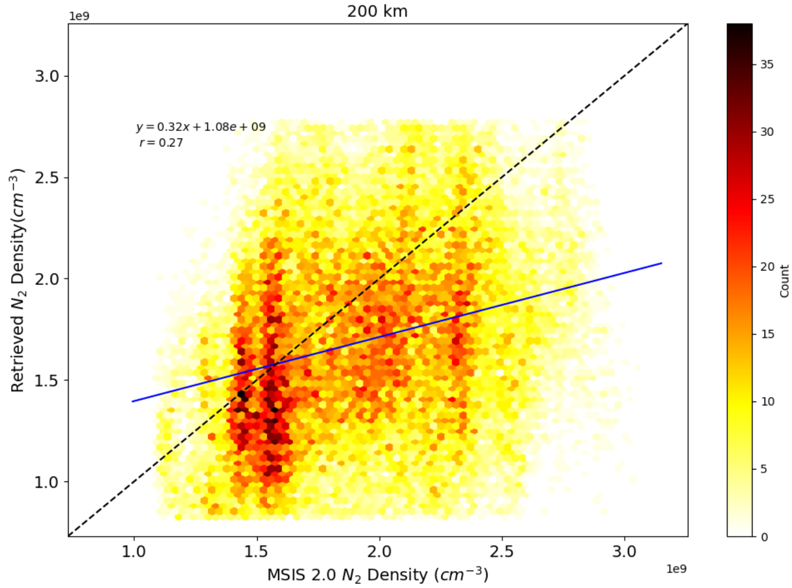

Fig. 22—Scatter density plot of retrieved and scaled MSIS 2.0 N_2 density at 200 km. Retrieved densities lower than the 5th and above the 95th percentiles have been excluded. The dashed black line indicates unity, while the solid blue line is a least-squares with parameters indicated in the top-left.

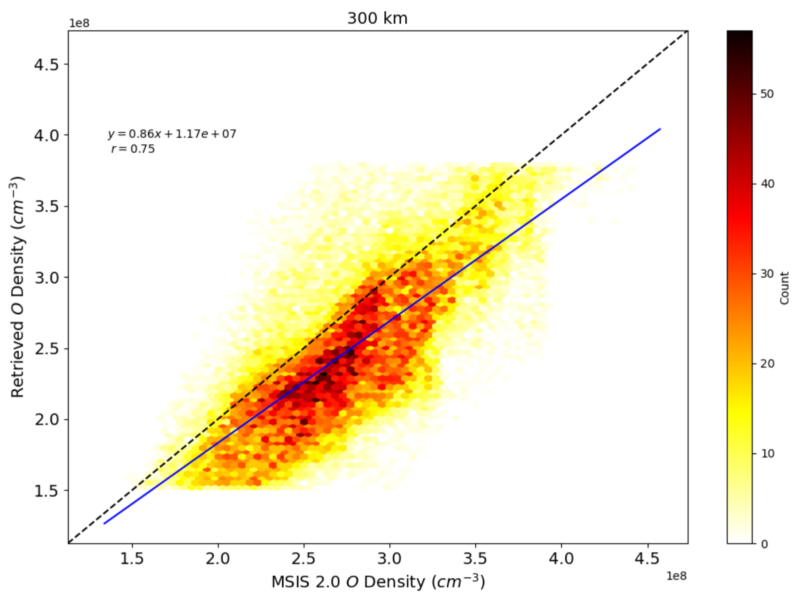

Fig. 23—Scatter density plot of retrieved and scaled MSIS 2.0 O density at 300 km. Retrieved densities lower than the 5th and above the 95th percentiles have been excluded. The dashed black line indicates unity, while the solid blue line is a least-squares with parameters indicated in the top-left.

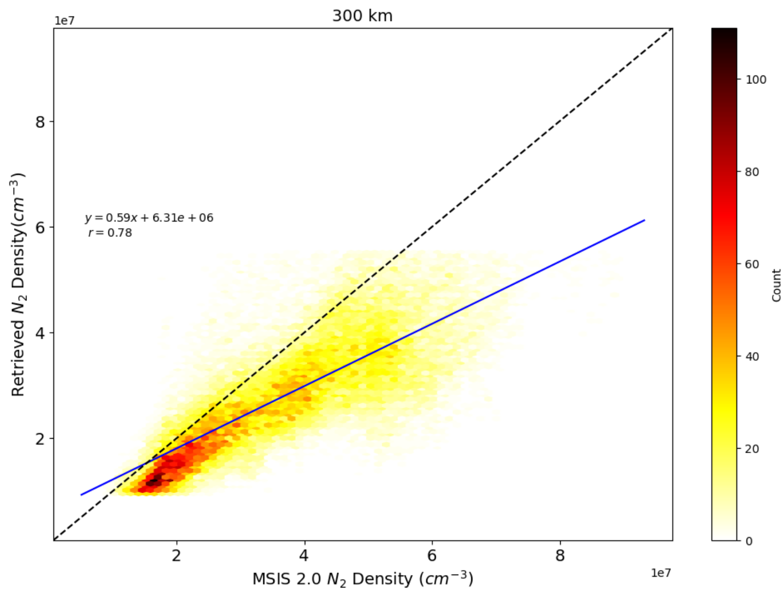

Fig. 24—Scatter density plot of retrieved and scaled MSIS 2.0 N_2 density at 300 km. Retrieved densities lower than the 5th and above the 95th percentiles have been excluded. The dashed black line indicates unity, while the solid blue line is a least-squares with parameters indicated in the top-left. Some non-linear behavior is visible, and the least-squares fit is dominated by the behavior at large densities.

with about the same strength as the MSIS 00 values at both altitudes. The least-squares fit at 300 km has a slope that is closer to unity than it was for MSIS 00. The changes implemented in MSIS 2.0 governing how O density varies between conditions are in agreement with the trend in the retrieval: namely, MSIS 00 under-estimates changes in O density.

The retrieved and MSIS 2.0 N_2 densities at 200 km show poor correlation. At 300 km, the correlation is stronger. At low densities, the slope on the scatter plot is near unity, indicating that MSIS 2.0 is in agreement with how N_2 density changes between observations. At high densities, the slope is lower. It is possible that two populations are represented or that there is a nonlinear effect in how N_2 observations relate to MSIS 2.0.

Figure 25 shows how the retrieved O and N_2 densities compare to MSIS 2.0 with local time at 250 km. The O difference has a local minimum around 13 LT and increases when approaching the terminator. The N_2 densities are the lowest relative to MSIS 2.0 in the evening. Of all our major sources of systematic uncertainty, the only one with a local time dependence is the g-factor scaling of the 86.5 nm and 87.8 nm lines. As the O 87.8 nm scalar increases with local time, it is possible the more of the brightness of the blended feature being attributed as originating from O leads to the decrease in measured N_2 density in the afternoon. In the case of O, it is unlikely that this is a result of systematic error in the retrieval; the 61.6 nm g-factor scalar is not LT dependent and 86.5 nm scalar has a LT dependence similar to the O density difference, which would likely increase estimated O density near the terminator. We are very possibly measuring a variation that is not present in MSIS 2.0.

Similarly, the variation in density at 250 km with latitude is shown in Fig. 26. The density of points is higher at the extreme latitudes because of the ICON viewing geometry. The retrieved O is noticeably higher

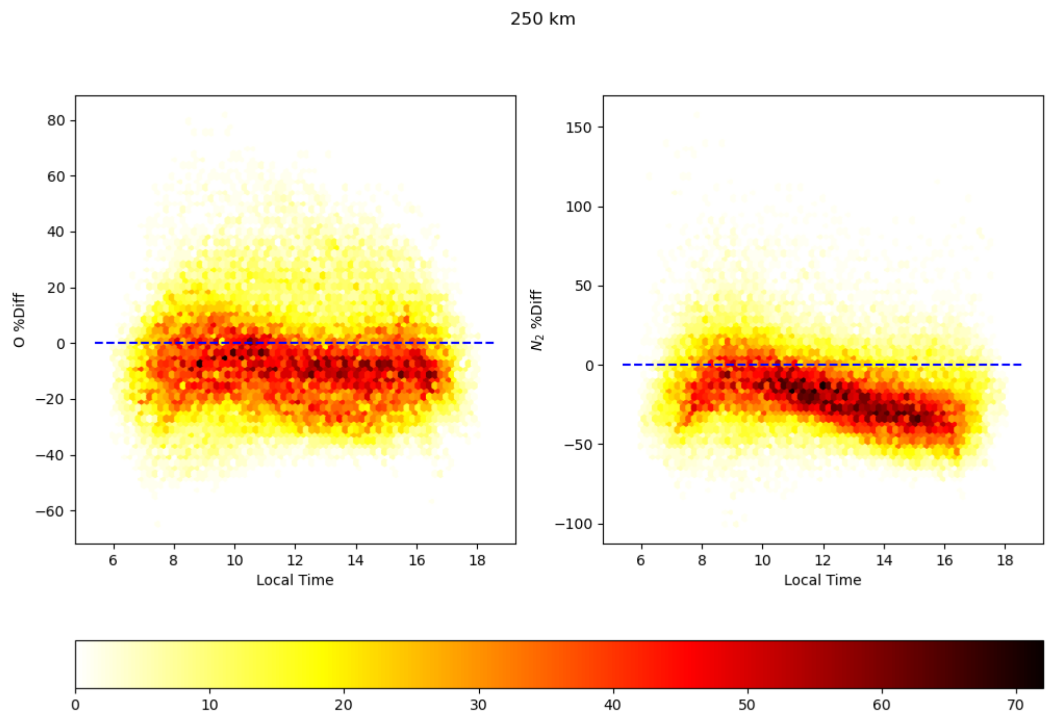

Fig. 25—Scatter density of O (left) and N_2 (right) percent difference from MSIS 2.0 vs. local time. Note that the y-axis scale differs between the two plots.

at higher latitudes compared to MSIS 2.0, while retrieved N_2 density compares about the same over the full latitude range. Figure 27 does not indicate any consistent dependence of the difference from MSIS 2.0 on solar F10.7 index, although the sample size of F10.7 higher than 75 sfu is small.

6.2 Comparison to SWARM Mass Density

As discussed in Section 1, recent neutral density measurements in the the 150-400 km range of our retrieval are not plentiful. Aside from the FUV derived measurements discussed in Section 6.3, there are virtually no remote sensing measurements of neutrals in this region. Just above this region, however, it is possible to make in-situ measurements of mass density derived from accelerometer or GNSS measured satellite drag. In this section, we compare the EUV retrieved densities to such measurements from SWARM-C.

The SWARM mission utilizes three satellites: SWARM-A, SWARM-B, and SWARM-C, which orbit at altitudes of approximately 460 km, 530 km, and 470 km, respectively. The SWARM neutral mass density product is derived from spacecraft accelerometer data and high fidelity gas-surface interaction modeling.[22] Of the two lower spacecraft, only SWARM-C has accelerometer-derived density as an available data product in 2020, so we compare to measurements from SWARM-C only.

The MSIS 00-driven framework provides a convenient and effective means to extend our measurements up to SWARM altitudes, as we need only report the densities on an extended altitude grid using the same

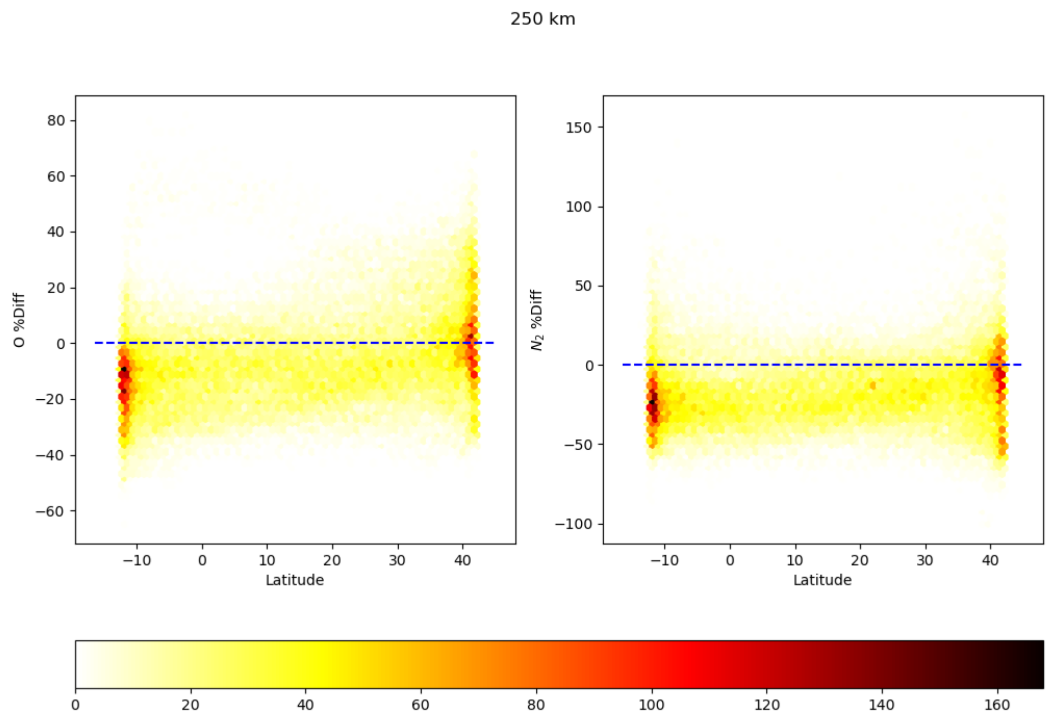

Fig. 26—Scatter density of O (left) and N_2 (right) percent difference from MSIS 2.0 vs. latitude. Note that the y-axis scale differs between the two plots.

retrieved scalars. We define a conjunction as a pair of SWARM and ICON EUV observations that occur within 5 degrees latitude, 5 degrees longitude, and 30 minutes of each other. We consider the EUV retrieved mass density to be the sum of the contributions from O and N_2 only, which should account for 90-95% of the mass density for a given exposure (according to MSIS 2.0).

Figure 28 shows the strong correlation between SWARM and EUV retrieval mass densities. For the majority of the data, the two measurements are very near equality. However, much of this strong correlation can be attributed to the fact that the retrieval has access to the MSIS climatology. In order to separate the measurement from the driving model, we have plotted the SWARM and EUV measurements less the MSIS 00 mass density (of O and N_2) in Fig. 29. The correlation is still strong and positive, indicating that we really are measuring some of the variation that SWARM sees. Of note is that the EUV retrieval is measuring higher densities than SWARM-C, despite the 5-10% of mass density missing from species other than O and N_2.

6.3 Comparison to ICON FUV and GOLD $\Sigma O/N_2$

The traditional means of satellite remote sensing of the neutral thermosphere is through the measurement of the N_2 Lyman-Birge-Hopfield band and O^+ 135.6 nm doublet in the far-UV (FUV) band of the electromagnetic spectrum. Most often these dayglow features are observed on the Earth's disk in nadir-viewing geometry and used to calculate the column O/N_2 ratio ($\Sigma O/N_2$). This quantity is defined as the ratio of

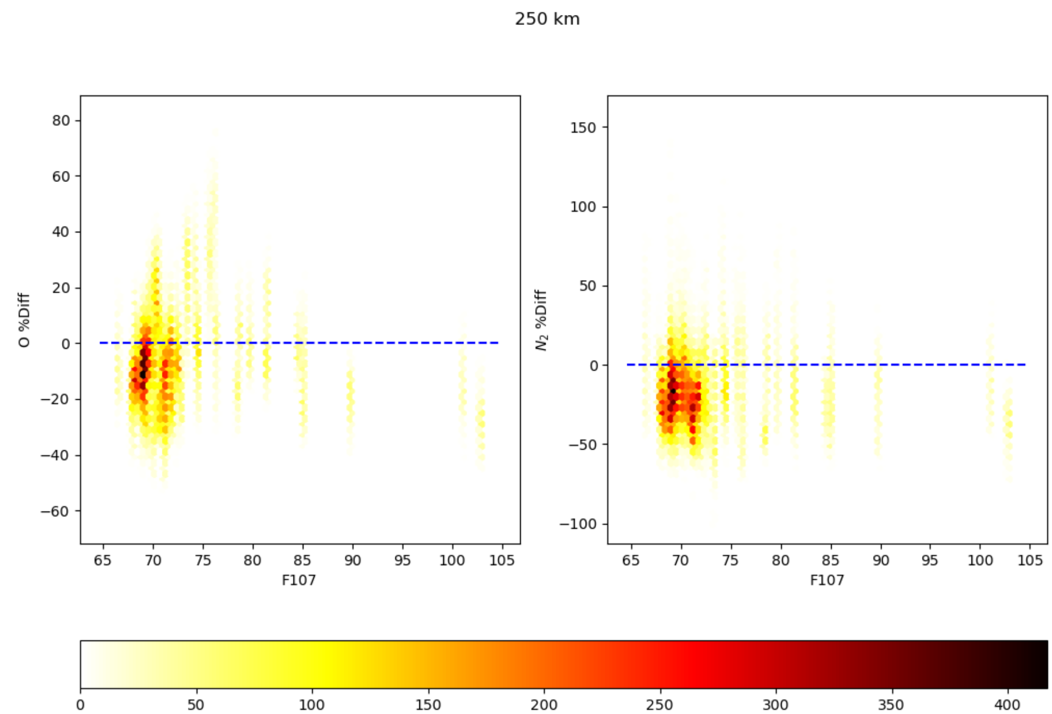

Fig. 27—Scatter density of O (left) and N_2 (right) percent difference from MSIS 2.0 vs. solar F10.7 index. Note that the y-axis scale differs between the two plots.

the column integrals of O and N_2 from the top of the thermosphere downwards until the N_2 column density reaches 10^{17} cm^{-2}; usually the altitude of this column base falls in the 130-140 km range.

$$\Sigma O/N_2 = \frac{\int_{z_{17}}^{\infty} n_O \, \mathrm{d}z}{\int_{z_{17}}^{\infty} n_{N_2} \, \mathrm{d}z} = \frac{\int_{z_{17}}^{\infty} n_O \, \mathrm{d}z}{10^{17}\mathrm{cm}^{-2}} \tag{13}$$

During 2020, this data product is available from GOLD and from ICON FUV. The retrieval algorithms for each of these products utilize a complex connection between the 135.6/LBH ratio and $\Sigma O/N_2$ dependent on factors such as solar EUV intensity and viewing geometry [6]; we will forego this and calculate an EUV $\Sigma O/N_2$ by integrating our retrieved MSIS 00 atmosphere according to Eq. (13). This approach has previously been used and validated with data from TIMED-GUVI.[4].

The ICON FUV instrument is a spectrographic imager with channels for LBH (near 157 nm) and 135.6 nm airglow. The imager measures 1D profiles on Earth's limb and disk.[23] The ICON 2.4 data product is daytime $\Sigma O/N_2$ measured on the disk using a DIT forward model retrieval. During the daytime, ICON FUV has similar north-viewing geometry to that of the EUV instrument. The instruments are not synchronized, but do utilize the same 12 second cadence.[9]

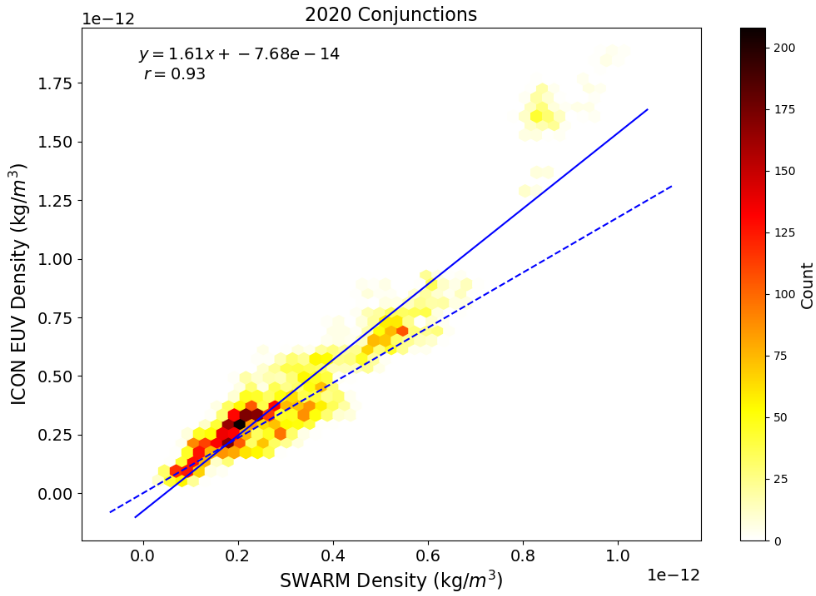

Fig. 28—SWARM-C accelerometer derived density and EUV derived mass density. EUV density includes only O and N_2, which make up about 95 % of total mass density at SWARM-C altitudes. The dashed blue line and plotted text indicate the least-squares fit and correlation coefficient of the data. The solid blue line represents equality between the data. The small high density population is clearly affecting the least-squares fit.

We have combined the EUV data into 60 second exposures, so for each EUV retrieval we take the closest (in time) FUV $\Sigma O/N_2$ measurement as a conjunction if it occurred within 60 seconds. There is a latitude offset of the EUV and FUV measurements, since the former comes from the limb and the latter the disk, but this remains an acceptable comparison.

The GOLD instrument is a two channel UV spectrograph which observes Earth's disk in the FUV from a geostationary orbit around the mouth of the Amazon river. During the daytime, GOLD takes 12 minute scans of the terrestrial disk, alternating between the northern and southern hemisphere. Column brightness of 135.6 nm and LBH 140.5-148.0 nm are converted to $\Sigma O/N_2$ using a lookup table constructed using MSIS 00, the NRLEUV solar spectrum model, and the AURIC airglow model. The resolution of the GOLD $\Sigma O/N_2$ product is about 1.8 degrees at nadir. [10][24]

We define a conjunction between GOLD and ICON EUV as a pair of observations that occur within 3.6 degrees latitude, 3.6 degrees longitude, and 1 hour of each other. If multiple GOLD pixels satisfy this criterion for a given EUV retrieval, we choose the pixel that minimizes the score defined as follows, where λ indicates longitude and ϕ latitude and Δ indicates the difference between the GOLD and EUV values:

$$\text{score} = (\frac{\Delta t}{1\text{ h}})^2 + (\frac{\Delta\lambda}{3.6\text{ degrees}})^2 + (\frac{\Delta\phi}{3.6\text{ degrees}})^2 \tag{14}$$

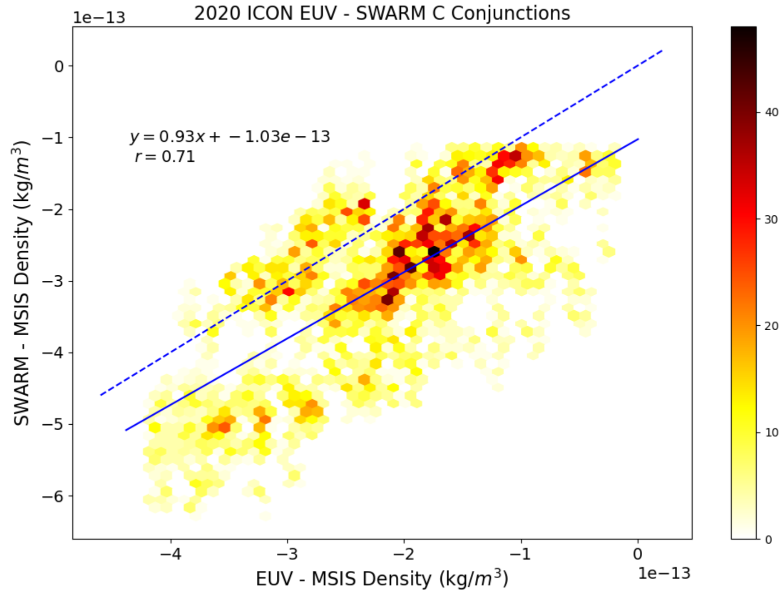

Fig. 29—SWARM-C accelerometer derived density and EUV derived mass density minus the mass density of O and N_2 from MSIS 00. EUV density includes only O and N_2, which make up about 95 % of total mass density at SWARM-C altitudes. The dashed blue line and plotted text indicate the least-squares fit and correlation coefficient of the data. The solid blue line represents equality between the data.

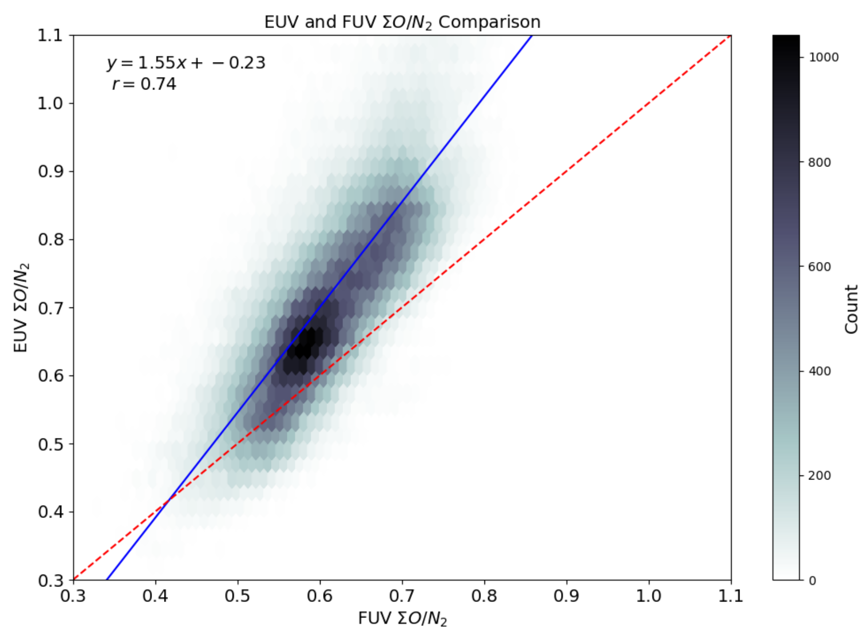

Fig. 30—Scatter plot showing the correlation between coincident measurements of ICON FUV and EUV O/N_2. The solid blue line and plotted text indicate the least-squares fit and correlation coefficient of the data. The dashed red line represents equality between the data.

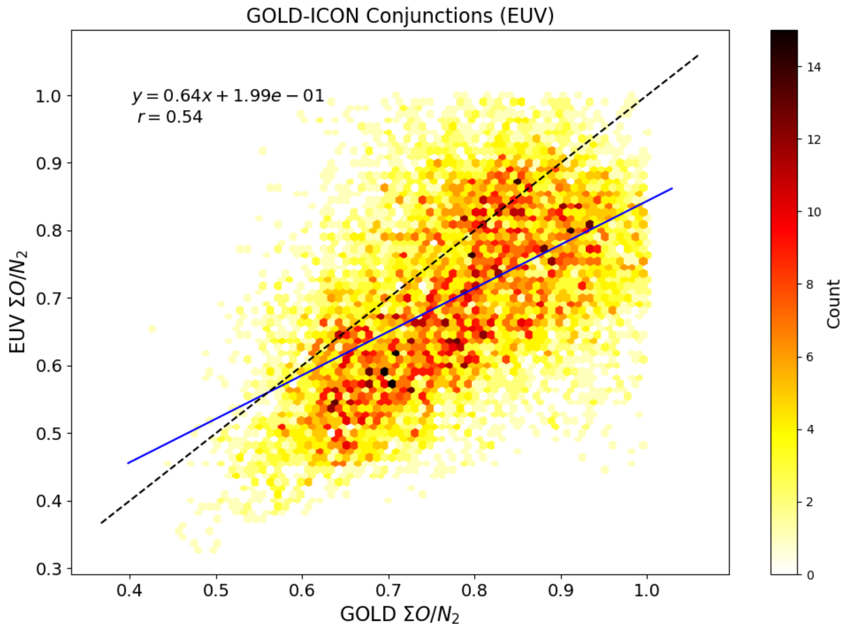

Fig. 31—Scatter plot showing the correlation between coincident measurements of GOLD and ICON EUV O/N_2. A small number of points have been removed by cutting out values greater than 1 for both GOLD and ICON EUV. The solid blue line and plotted text indicate the least-squares fit and correlation coefficient of the data. The dashed black line represents equality between the data.

Figure 30 and Fig. 31 contain $\Sigma O/N_2$ scatter density plots of ICON EUV, ICON FUV, and GOLD, respectively. The ICON EUV retrieval correlates well with each of the other measurements, especially given the relatively loose conjunction definition used for ICON EUV and GOLD observations. Interestingly, ICON EUV retrieved $\Sigma O/N_2$ typically exceeds the ICON FUV value but is less than the GOLD value. The ICON EUV retrieval seems similarly calibrated to GOLD and is noticeably more sensitive than ICON FUV.

A difference between the EUV and FUV $\Sigma O/N_2$ is to be expected since EUV always observes a higher latitude; however, Figs. 32 – 33 show that the difference does not reverse with season, which would occur if the discrepancy came solely from the latitude offset. Figure 33 provides a useful visualization of the different $\Sigma O/N_2$ measurements vary throughout the year. Each source has its problem days, but for the most part they follow the same trend. Some notable exceptions occur, such as when ICON EUV and FUV trend opposite of GOLD around the beginning of March, or when FUV experiences dips in November and December that are not noticeable in GOLD or EUV. Lastly, we note that for one day, November 1, the EUV median $\Sigma O/N_2$ of 1.4 lies beyond the chart limits as presented here.

7. EFFECTS OF USING THE CORRECTED 61.6 NM DATA

Here we discuss the effect of using the alternate retrieval which utilizes the 61.6 nm data correction described in Section 4.3.2. Figure 34 shows the full distribution of retrieved F10.7, O density, and N_2 density scalars just as in Fig. 12. Whereas the original retrieval was fit to F10.7 scalars just below unity, the corrected retrieval has F10.7 scalars peaking just above unity. Perhaps unsurprisingly, the increase in 61.6

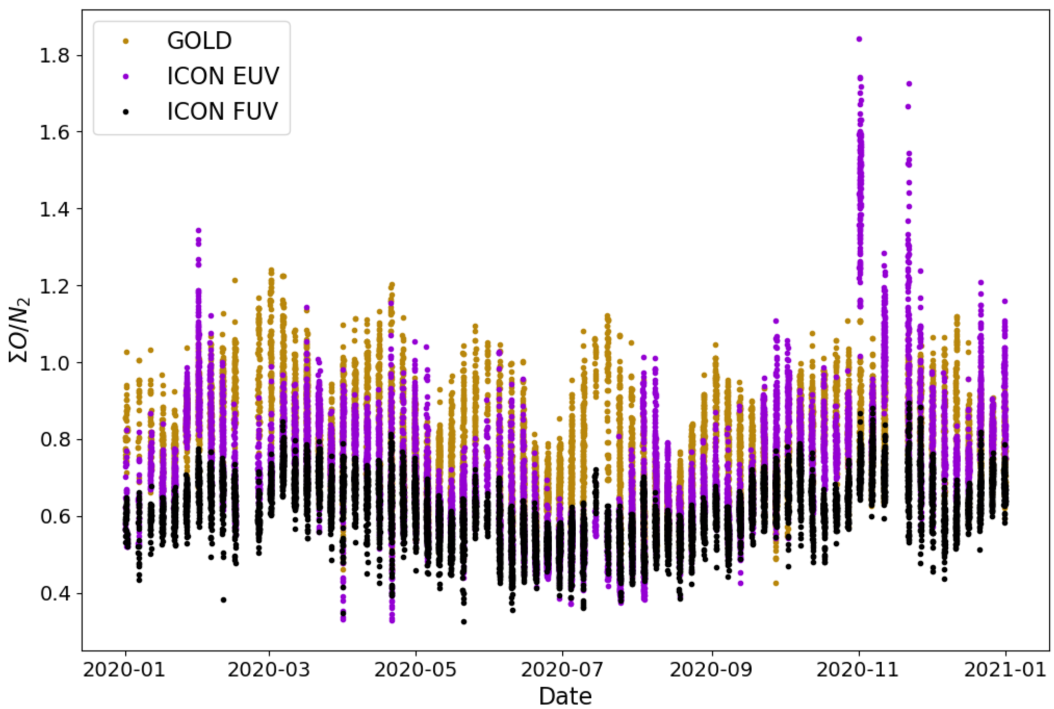

Fig. 32—Time series of all coincident measurements of $\Sigma O/N_2$ from GOLD (gold), ICON EUV (purple), and ICON FUV (black).

nm brightness at high altitudes yields an expanded atmosphere. This can be seen to a lesser degree when comparing Fig. 37 to Fig. 28, as the former shows increased residuals from MSIS density.

Perhaps to compensate for the increased scale height, the corrected retrieval settles on lower values of O and N_2 density scalars. The change is most noticeable in the O density scalar, as the original retrieval already showed N_2 density scalars below the baseline of 0.85.

Comparison to MSIS 00 and MSIS 2.0 in Fig. 35 indicates that the corrected retrieval shows the opposite trend as the original with altitude. That is, the density of both species increases relative to both models at high altitudes. This suggests that the correction is perhaps an over-correction.

The strangest effect of using corrected data in the retrieval can be seen in Fig. 36, which compares the correlation to FUV O/N_2 between the uncorrected and corrected retrievals. The correction introduces a non-linear effect, which causes EUV O/N_2 to more closely follow the FUV at higher values. This is certainly fascinating, and appears to be an improvement to the eye. However, the uncorrected values could be made to compare to the FUV with a simple calibration, while calibrating the corrected O/N_2 would be more complex.

Finally, Fig. 37 shows the correlation of residuals from MSIS 00 for the corrected retrieval and SWARM. Compared to Fig. 29, the values in Fig. 37 are slightly further from unity. However, more significant and quantitative is that the correlation is weaker for the corrected retrieval.

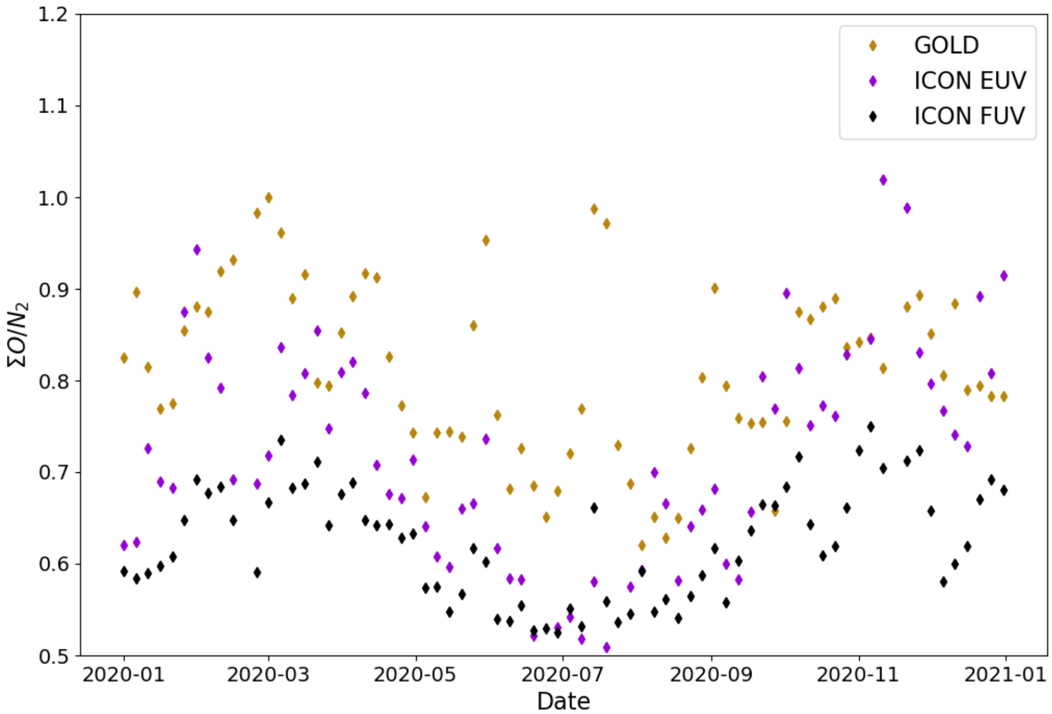

Fig. 33—Time series of daily median $\Sigma O/N_2$ from GOLD (gold), ICON EUV (purple), and ICON FUV (black).

The correction was a helpful experiment as it shows that the retrieval is sensitive to the 61.6 nm values at high altitude. However, we do not consider the results convincing enough to make this the default retrieval. It is inconclusive whether some bias in MSIS 00 is dominant over whatever systematic error may exist in the O g-factors or 61.6 nm data.

8. DISCUSSION

In this report, we have discussed the development of an algorithm to measure thermospheric O and N_2 density using limb measurements of airglow at 61.6 nm and 87.8 nm from the ICON EUV instrument. This began with the development of an EUV airglow forward model, which predicts an EUV airglow profile at a given wavelength. Production is modeled using scaled g-factors from the well-established AURIC model, which form the basis for the existing ICON EUV ionosphere retrieval algorithm. Transport modeling considers pure absorption by neutrals. Neither the g-factors nor the cross sections are published with uncertainties, and each is a significant source of systematic uncertainty in the forward model and retrieval.

The forward model was used to perform a detailed study of the dayglow near 87.8 nm, which has seen little study outside of this work and its predecessor [2]. The emissions are identified to be a blend of the O 87.8 nm line and a nearby N or N^+ feature. A survey was conducted over the ICON EUV measurements in 2020 to determine the best-fit g-factor scaling as a function of season and local time. This is another major source of systematic uncertainty. The lack of specific identification of the N/N^+ is a comparatively minor

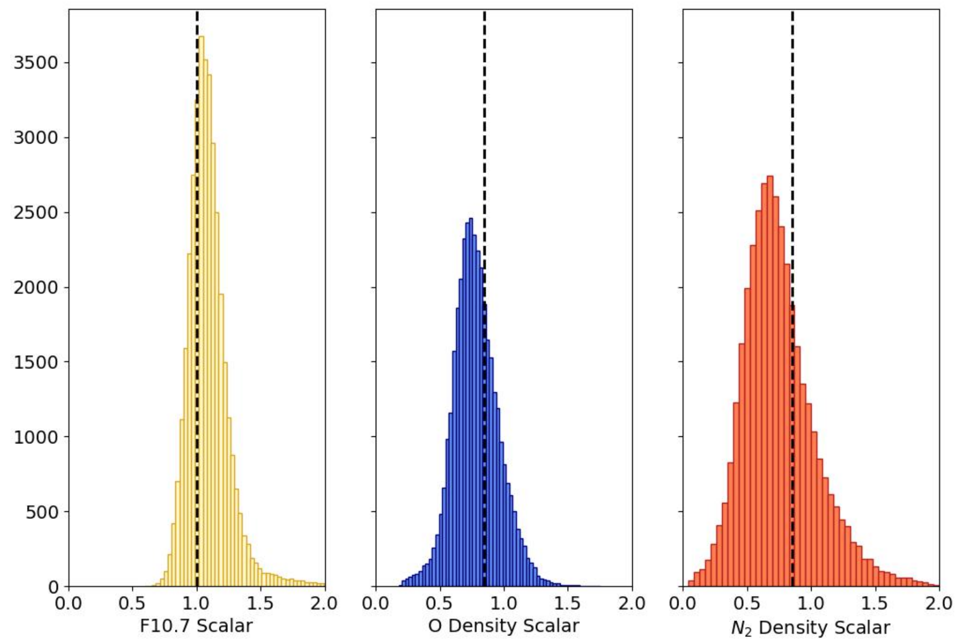

Fig. 34—Distribution of F107, O, and N_2 scalars for all retrievals using the corrected 61.6 nm data in 2020. The dotted line indicates the initial value, 1.0 for F10.7 and 0.85 for the density scalars. (These values of 1.0 and 0.85 are respectively used in order to determine the g-factors.) See Fig. 12 for comparison.

source of uncertainty, since absorption cross-sections vary a non-negligible but small amount over the range of possible wavelengths.

The forward model is inverted using the well established and studied Discrete Inverse Theory. This is done by scaling three aspects of the MSIS 00 atmospheric model: input solar F10.7 flux and output O and N_2 density. Here the retrieval inherits systematic uncertainty in the ICON EUV data and from any systematic biases in the MSIS 00 model that would render the inverse method unable to converge to the true atmospheric state. These factors are relative minor compared to the contributions to systematic uncertainty discussed in the previous paragraphs.

The retrieval output is physically plausible and compares reasonably to the MSIS 00 and MSIS 2.0 models. The most significant trend is that the retrieved atmospheres are cooler with smaller scale heights compared to the models. It is worth noting that thermospheric temperature modeling has not been significantly updated in MSIS since MSIS 00, meaning that MSIS 2.0 lacks temperature input from around the low solar minimum in 2020.

The retrieval compares favorably to coincident measurements from multiple satellite-based instruments. Comparisons to mass densities derived from acclerometer-determined satellite drag on SWARM-C show that the two measurements show strong correlation before and after correcting for the EUV retrieval's access to the MSIS climatology.

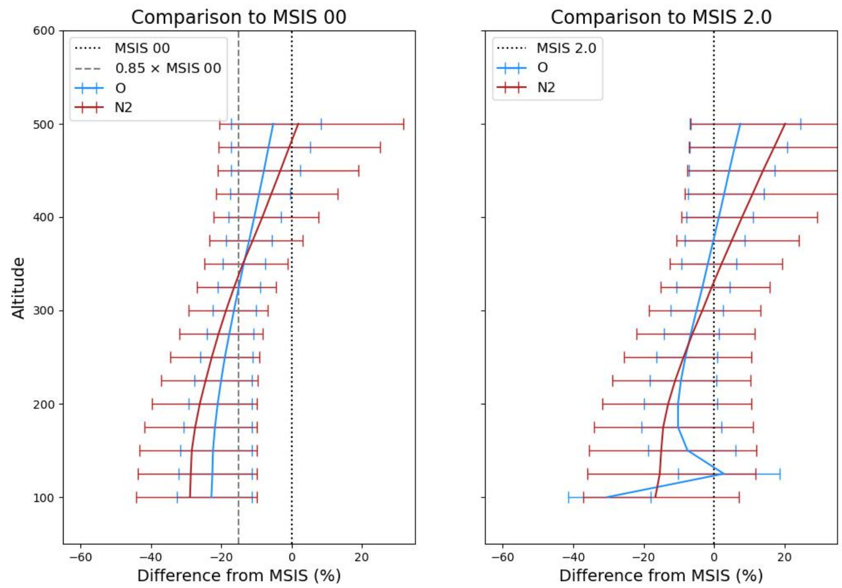

Fig. 35—The median difference (%) between the retrievals and MSIS 00 (left) and MSIS 2.0 (right). Error bars represent the upper and lower quartiles. The MSIS 00 plot indicates 85% of the MSIS 00 O and N_2 density, which are the values used to determine the g-factor scaling. Compare Fig. 13

EUV derived measurements of $\Sigma O/N_2$ correlate strongly with FUV derived measurements on the same spacecraft, although the EUV values respond more sensitively to changes in atmospheric state. ICON EUV measurements of $\Sigma O/N_2$ are generally higher than that from ICON FUV; however, they are generally lower than what is seen by the GOLD instrument from GEO. Additionally, GOLD and EUV retrievals of $\Sigma O/N_2$ show similar sensitivity. All three measurements of $\Sigma O/N_2$ show comparable variation on daily and seasonal timescales.

The initial favorable comparison to other measurements from this retrieval algorithm encourages several areas for continuing development. One key aspect that remains is a rigorous characterization of retrieval uncertainty. This could would be helpful in its various degrees of rigor: direct propagation of estimated contributing uncertainties, a sensitivity study, or a full Monte Carlo simulation study would all contribute to generating a more fully validated data product. Some experiments intended to identify and correct for systematic biases in the g-factors or airglow measurements have been conducted (see Section 4.3.2 and Section 7) but are inconclusive at this time.

Further experimental results could also be used to improve the retrieval. The release of the ICON FUV limb neutral densities will be very helpful for improved validation. High resolution cross-sections, such as the ones provided to us for atomic O would help to reduce systematic uncertainty, as would higher resolution measurements of EUV airglow that are sensitive in the 87.8 nm region.

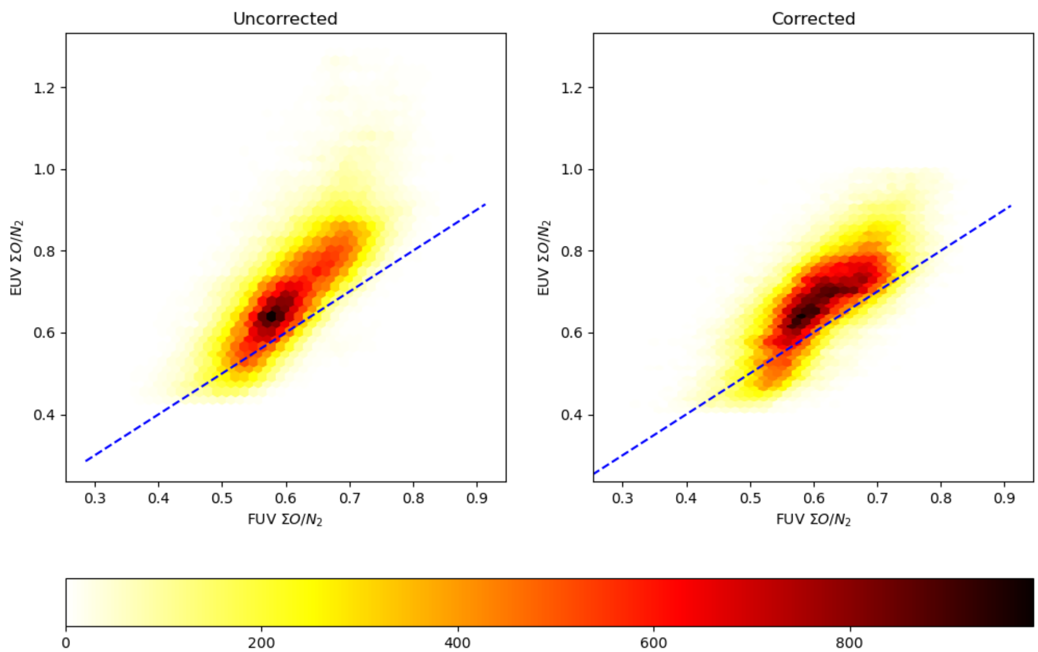

Fig. 36—Scatters plot showing the correlation between coincident measurements of ICON FUV and EUV O/N_2 with the uncorrected (left) and corrected (right) 61.6 nm data. The dashed red line represents equality between the data.

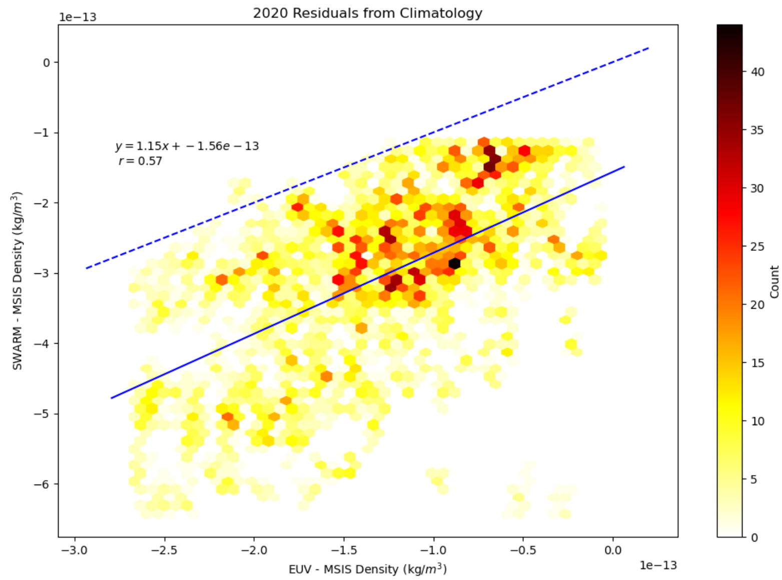

Fig. 37—SWARM-C accelerometer derived density and EUV derived mass density (from corrected 61.6 nm data) minus the mass density of O and N_2 from MSIS 00. The dashed blue line and plotted text indicate the least-squares fit and correlation coefficient of the data. The solid blue line represents equality between the data. Compare Fig. 29.

REFERENCES

1. T. W. Fang, A. Kubaryk, D. Goldstein, Z. Li, T. Fuller-Rowell, G. Millward, H. J. Singer, R. Steenburgh, S. Westerman, and E. Babcock, "Space Weather Environment During the SpaceX Starlink Satellite Loss in February 2022," *Space Weather* **20**(11), e2022SW003193 (2022), doi:https://doi.org/10.1029/2022SW003193. URL `https://agupubs.onlinelibrary.wiley.com/doi/abs/10.1029/2022SW003193`, e2022SW003193 2022SW003193.

2. R. M. Tuminello, S. L. England, M. M. Sirk, R. R. Meier, A. W. Stephan, E. J. Korpela, T. J. Immel, S. B. Mende, and H. U. Frey, "Neutral Composition Information in ICON EUV Dayglow Observations," *Journal of Geophysical Research: Space Physics* **127**(8), e2022JA030592 (2022), doi:https://doi.org/10.1029/2022JA030592. URL `https://agupubs.onlinelibrary.wiley.com/doi/abs/10.1029/2022JA030592`, e2022JA030592 2022JA030592.

3. J. T. Emmert, D. P. Drob, J. M. Picone, D. E. Siskind, M. Jones Jr., M. G. Mlynczak, P. F. Bernath, X. Chu, E. Doornbos, B. Funke, L. P. Goncharenko, M. E. Hervig, M. J. Schwartz, P. E. Sheese, F. Vargas, B. P. Williams, and T. Yuan, "NRLMSIS 2.0: A Whole-Atmosphere Empirical Model of Temperature and Neutral Species Densities," *Earth and Space Science* **8**(3), e2020EA001321 (2021), doi:https://doi.org/10.1029/2020EA001321. URL `https://agupubs.onlinelibrary.wiley.com/doi/abs/10.1029/2020EA001321`, e2020EA001321 2020EA001321.

4. R. R. Meier, J. M. Picone, D. Drob, J. Bishop, J. T. Emmert, J. L. Lean, A. W. Stephan, D. J. Strickland, A. B. Christensen, L. J. Paxton, D. Morrison, H. Kil, B. Wolven, T. N. Woods, G. Crowley, and S. T. Gibson, "Remote Sensing of Earth's Limb by TIMED/GUVI: Retrieval of thermospheric composition and temperature," *Earth and Space Science* **2**(1), 1–37 (2015), doi:https://doi.org/10.1002/2014EA000035. URL `https://agupubs.onlinelibrary.wiley.com/doi/abs/10.1002/2014EA000035`.

5. D. J. Strickland, J. S. Evans, and L. J. Paxton, "Satellite remote sensing of thermospheric O/N_2 and solar EUV. 1. Theory," *Journal of Geophysical Research* **100**(A7), 12217–12226 (July 1995), doi:10.1029/95JA00574.

6. R. R. Meier, "The Thermospheric Column O/N_2 Ratio," *Journal of Geophysical Research* **126**(3), e29059 (Mar. 2021), doi:10.1029/2020JA029059.

7. G. W. Prölss and M. K. Bird, *Physics of the Earth's Space Environment: an introduction* (Springer, Berlin, 2004).

8. J. S. Evans, D. J. Strickland, and R. E. Huffman, "Satellite remote sensing of thermospheric O/N_2 and solar EUV. 2. Data analysis," *Journal of Geophysical Research* **100**(A7), 12227–12234 (July 1995), doi:10.1029/95JA00573.

9. A. W. Stephan, R. R. Meier, S. L. England, S. B. Mende, H. U. Frey, and T. J. Immel, "Daytime O/N_2 Retrieval Algorithm for the Ionospheric Connection Explorer (ICON)," *Space Science Reviews* **214**(1), 42 (Feb. 2018), doi:10.1007/s11214-018-0477-6.

10. J. Correira, J. S. Evans, J. D. Lumpe, A. Krywonos, R. Daniell, V. Veibell, W. E. McClintock, and R. W. Eastes, "Thermospheric Composition and Solar EUV Flux From the Global-Scale Observations of the Limb and Disk (GOLD) Mission," *Journal of Geophysical Research (Space Physics)* **126**(12), e29517 (Dec. 2021), doi:10.1029/2021JA029517.

11. T. J. Immel, S. L. England, S. B. Mende, R. A. Heelis, C. R. Englert, J. Edelstein, H. U. Frey, E. J. Korpela, E. R. Taylor, W. W. Craig, S. E. Harris, M. Bester, G. S. Bust, G. Crowley, J. M. Forbes, J. C. Gérard, J. M. Harlander, J. D. Huba, B. Hubert, F. Kamalabadi, J. J. Makela, A. I. Maute, R. R. Meier, C. Raftery, P. Rochus, O. H. W. Siegmund, A. W. Stephan, G. R. Swenson, S. Frey, D. L. Hysell, A. Saito, K. A. Rider, and M. M. Sirk, "The Ionospheric Connection Explorer Mission: Mission Goals and Design," *Space Science Reviews* **214**(1), 13 (Feb. 2018), doi:10.1007/s11214-017-0449-2.

12. M. M. Sirk, E. J. Korpela, Y. Ishikawa, J. Edelstein, E. H. Wishnow, C. Smith, J. McCauley, J. B. McPhate, J. Curtis, T. Curtis, S. R. Gibson, S. Jelinsky, J. A. Lynn, M. Marckwordt, N. Miller, M. Raffanti, W. Van Shourt, A. W. Stephan, and T. J. Immel, "Design and Performance of the ICON EUV Spectrograph," *Space Science Reviews* **212**(1-2), 631–643 (Oct. 2017), doi:10.1007/s11214-017-0384-2.

13. A. W. Stephan, E. J. Korpela, M. M. Sirk, S. L. England, and T. J. Immel, "Daytime Ionosphere Retrieval Algorithm for the Ionospheric Connection Explorer (ICON)," *Space Science Reviews* **212**(1-2), 645–654 (Oct. 2017), doi:10.1007/s11214-017-0385-1.

14. A. W. Stephan, J. M. Picone, S. A. Budzien, R. L. Bishop, A. B. Christensen, and J. H. Hecht, "Measurement and application of the O II 61.7 nm dayglow," *Journal of Geophysical Research (Space Physics)* **117**(A1), A01316 (Jan. 2012), doi:10.1029/2011JA016897.

15. R. R. Meier and J. M. Picone, "Retrieval of absolute thermospheric concentrations from the far UV dayglow: An application of discrete inverse theory," *Journal of Geophysical Research: Space Physics* **99**(A4), 6307–6320 (1994), doi:https://doi.org/10.1029/93JA02775. URL `https://agupubs.onlinelibrary.wiley.com/doi/abs/10.1029/93JA02775`.

16. J. M. Picone, R. R. Meier, O. A. Kelley, D. J. Melendez-Alvira, K. F. Dymond, R. P. McCoy, and M. J. Buonsanto, "Discrete inverse theory for 834-Å ionospheric remote sensing," *Radio Science* **32**(5), 1973–1984 (1997), doi:https://doi.org/10.1029/97RS01028. URL `https://agupubs.onlinelibrary.wiley.com/doi/abs/10.1029/97RS01028`.

17. D. J. Strickland, J. Bishop, J. S. Evans, T. Majeed, P. M. Shen, R. J. Cox, R. Link, and R. E. Huffman, "Atmospheric ultraviolet radiance integrated code (AURIC): theory, software architecture, inputs, and selected results.," *Journal of Quantitative Spectroscopy & Radiative Transfer* **62**(6), 689–742 (Aug. 1999), doi:10.1016/S0022-4073(98)00098-3.

18. R. Conway, "Photoabsorption and Photoionization Cross Sections of O, O2, and N2 for Photoelectron Production Calculations: A Compilation of Recent Laboratory Measurements," NRL Memorandum NRL/MR/6155, Naval Research Laboratory, Washington, DC, Mar. 1988.

19. A. Kramida, Yu. Ralchenko, J. Reader, and and NIST ASD Team," NIST Atomic Spectra Database (ver. 5.9), [Online]. Available: `https://physics.nist.gov/asd` [2022, July 18]. National Institute of Standards and Technology, Gaithersburg, MD., 2021.

20. E. P. Gentieu, P. D. Feldman, R. W. Eastes, and A. B. Christensen, "EUV airglow during active solar conditions: 2. Emission between 530 and 930 Å," *Journal of Geophysical Research: Space Physics* **89**(A12), 11053–11058 (1984), doi:https://doi.org/10.1029/JA089iA12p11053. URL `https://agupubs.onlinelibrary.wiley.com/doi/abs/10.1029/JA089iA12p11053`.

21. J. T. Emmert, J. M. Picone, and R. R. Meier, "Thermospheric global average density trends, 1967–2007, derived from orbits of 5000 near-Earth objects," *Geophysical Research Letters* **35**(5) (2008), doi:https://doi.org/10.1029/2007GL032809. URL `https://agupubs.onlinelibrary.wiley.com/doi/abs/10.1029/2007GL032809`.

22. G. March, J. van den IJssel, C. Siemes, P. N. A. M. Visser, E. N. Doornbos, and M. Pilinski, "Gas-surface interactions modelling influence on satellite aerodynamics and thermosphere mass density," *Journal of Space Weather and Space Climate* **11**, 54 (Sept. 2021), doi:10.1051/swsc/2021035.

23. S. B. Mende, H. U. Frey, K. Rider, C. Chou, S. E. Harris, O. H. W. Siegmund, S. L. England, C. Wilkins, W. Craig, T. J. Immel, P. Turin, N. Darling, J. Loicq, P. Blain, E. Syrstad, B. Thompson, R. Burt, J. Champagne, P. Sevilla, and S. Ellis, "The Far Ultra-Violet Imager on the Icon Mission," **212**(1-2), 655–696 (Oct. 2017), doi:10.1007/s11214-017-0386-0.

24. R. W. Eastes, W. E. McClintock, A. G. Burns, D. N. Anderson, L. Andersson, M. Codrescu, J. T. Correira, R. E. Daniell, S. L. England, J. S. Evans, J. Harvey, A. Krywonos, J. D. Lumpe, A. D. Richmond, D. W. Rusch, O. Siegmund, S. C. Solomon, D. J. Strickland, T. N. Woods, A. Aksnes, S. A. Budzien, K. F. Dymond, F. G. Eparvier, C. R. Martinis, and J. Oberheide, "The Global-Scale Observations of the Limb and Disk (GOLD) Mission," **212**(1-2), 383–408 (Oct. 2017), doi:10.1007/s11214-017-0392-2.